Brigham Young University
BYU ScholarsArchive

All Theses and Dissertations

2017-07-01

High-Voltage Measurements Using Slab-Coupled Optical Sensors

LeGrand Jared Shumway
Brigham Young University

Follow this and additional works at: https://scholarsarchive.byu.edu/etd

 Part of the Electrical and Computer Engineering Commons

BYU ScholarsArchive Citation

Shumway, LeGrand Jared, "High-Voltage Measurements Using Slab-Coupled Optical Sensors" (2017). *All Theses and Dissertations*. 6499.
https://scholarsarchive.byu.edu/etd/6499

This Thesis is brought to you for free and open access by BYU ScholarsArchive. It has been accepted for inclusion in All Theses and Dissertations by an authorized administrator of BYU ScholarsArchive. For more information, please contact scholarsarchive@byu.edu, ellen_amatangelo@byu.edu.

High Voltage Measurements Using Slab-Coupled Optical Sensors

LeGrand Jared Shumway

A thesis submitted to the faculty of
Brigham Young University
in partial fulfillment of the requirements for the degree of

Master of Science

Stephen Schultz, Chair
Aaron Hawkins
Daniel Smalley

Department of Electrical and Computer Engineering

Brigham Young University

Copyright © 2017 LeGrand Jared Shumway

All Rights Reserved

ABSTRACT

High Voltage Measurements Using Slab-Coupled Optical Sensors

LeGrand Jared Shumway
Department of Electrical and Computer Engineering, BYU
Master of Science

This work highlights slab coupled optical sensors (SCOS) and their ability to measure high voltages. Although other high voltage measurement techniques exist, most of these techniques are electrical devices and are therefore more susceptible to stray ground currents and other electromagnetic interferences (EMI), which may cause signal distortion. Optical sensors are less susceptible to such interferences and these sensors, such as the Pockels cell, have been used in measuring high voltage. SCOS offer an alternative method of measuring high voltage optically. Consisting of an optical fiber and an electro-optic slab waveguide, SCOS have the advantage of being very small in size (0.2 mm x 0.3 mm cross-section), simpler composition, and potentially less coupling losses.

Issues associated with high voltage measurements are addressed such as unwanted corona, arcing, and EMI. Solutions are also explored which include insolating materials, electrode geometries, Faraday cages, and using optical sensors such as SCOS.

Although the SCOS has been traditionally used to measure electric field, the SCOS is able to measure high voltage through the use of an electrode structure. The SCOS' ability to measure high voltage is showcase through the construction and output measurements of several high voltage systems: an ignition coil-based circuit, a dual ignition coil circuit, a Marx generator, and a 200 kV generator used in a capacitor discharge configuration. These measurements show the SCOS' ability to measure at least 111 kV capacitor discharges with 6.6 ns rise times and other various high voltage waveforms.

Keywords: slab coupled optical sensors, optical sensing, high voltage measurements

ACKNOWLEDGEMENTS

I would like to thank Dr. Schultz for his friendship and guidance as an undergraduate and especially as a graduate student. He has been an excellent source of direction and support over the years. I would also like to thank Frederick Seng, Nikola Stan, Spencer Chadderdon, and Dr. Richard Selfridge for their guidance, mentoring, and support in the lab as well as my other coworkers in the BYU Optics lab. You have all made this work possible and I can't thank you enough for the support. I would like to thank the U. S. Department of Defense for funding as well as KVH industries for their donations in conjunction with this research.

TABLE OF CONTENTS

LIST OF TABLES

LIST OF FIGURES

1 INTRODUCTION

This thesis highlights my contribution of using slab coupled optical sensors (SCOS) to measure high voltage (HV) systems. Traditional high voltage measurement techniques are discussed as well as a brief SCOS background. Problems associated with high voltage measurements are also addressed. Three different HV systems were constructed: a Marx generator, a 200kV Pulse Generator, and an automotive ignition coil circuit. SCOS are used to measure the output of each constructed circuit. A voltage divider circuit is also used to measure the automotive ignition coil circuit, which shows how some traditional electrical high voltage measurement techniques might lead to unwanted measurement error.

1.1 Contributions

Through my research in the Optics Lab at Brigham Young University, I have made the following contributions:

Major Contributions:

- Construction, research, and measurements of various high voltage systems including: various Marx generators, single and dual ignition coil circuits, 200 kV arc discharge circuit, capacitor discharge circuits [1,2]
- Research of high voltage systems and decreasing measurement problems associated with them (Section 4)

- Created electrode structure implemented for SCOS measurements (Section 4.4) [1,2]
- Characterization of the electric fields within ion traps [3,4]
- Implemented the recursive random sample consensus (RRANSAC) method to peak track multiplexed fiber bragg gratings (FBGs)

Minor Contributions:

- Developing push-pull SCOS [5,6]
- Improving methods by which SCOS can be used in harsh environments [7,8]
- Improving method of taking nonlinear SCOS measurements [9,10]
- Characterization of strain on a Hopkinson bar specimen using an FBG [11]
- Measuring arc dynamics [12]
- Non-intrusive voltage measurements in coaxial cable [13]
- Development testing on Antenna SCOS for increased sensitivity [14]

2 HIGH VOLTAGE MEASUREMENT TECHNIQUES

2.1 Brief History of Electrical High Voltage Measurement Techniques

High voltage measurement systems take on various forms and applications. The nature of the voltage in question determines the device needed for measuring the system.

2.1.1 Alternating Current (AC)

Sphere gaps, capacitive voltage dividers, and voltage transformers are often used to measure high voltage AC signals [1,16]. Sphere gaps consist of adjacent sphere electrodes separated by a given distance. When a fairly homogenous gap material, the geometry of the sphere electrodes and gap spacing can be adjusted so that arcing only occurs when the voltage between the electrodes is beyond a designed amplitude [16]. Certain capacitive voltage divider configurations exist which essentially scale the voltage down to a measureable level, and then implement a rectifier circuit to record the peak value of the scaled-down AC voltage [1]. For a given frequency to be measured, system components can be chosen to accurately measure the peak value of the desired system.

2.1.2 Direct Current (DC)

DC voltages are perhaps the simplest voltages to measure. Voltage dividers, and electrostatic voltmeters are often used due to the static nature of the measurement.

Voltage dividers can be purely capacitive, resistive, or a combination of both. Dividers are perhaps the simplest devices used to measure high voltage systems, due to their relatively simple construction. Regardless of the nature of the device, each voltage divider operates on the same basic principle: scaling the high voltage of the system to a lower voltage which can then be measured by standard electronics such as a common oscilloscope or voltmeter. This recorded voltage is a scaled replication of the actual high voltage output.

Electrostatic voltmeters are based on the principle that when two plane disk electrodes have a voltage potential applied between them, there is a force between them. For a given structure, this force can be measured and the applied voltage can then be inferred. One of the biggest advantages to such devices is that there are minimal loading problems associated with the device [16].

2.1.3 Pulse Voltages

For pulse voltages, voltage dividers are often used [17,18,5]. Although designing these devices to measure pulse voltages takes great care and expertise, such dividers are capable of measuring very fast rise times, some even reporting speeds of sub-nanosecond response [18]. Figure 2-1 shows an example of such device.

2.1.4 Problems Associated with Electrically Measuring HV Systems

Higher voltage signals have higher associated electromagnetic (EM) fields, which often introduce unwanted electrical noise in measurements. This unwanted electromagnetic interference (EMI) is often caused by stray ground currents and electrical coupling within wires [20,21,22,23]. Due to the presence of this unwanted EMI, high voltage and high current measurements taken using electrical voltage sensors and connectors are often susceptible to

distortion and inaccuracies [21,22,23]. Moreover, using electrical sensors to characterize a high voltage system might result in accidental equipment damage.

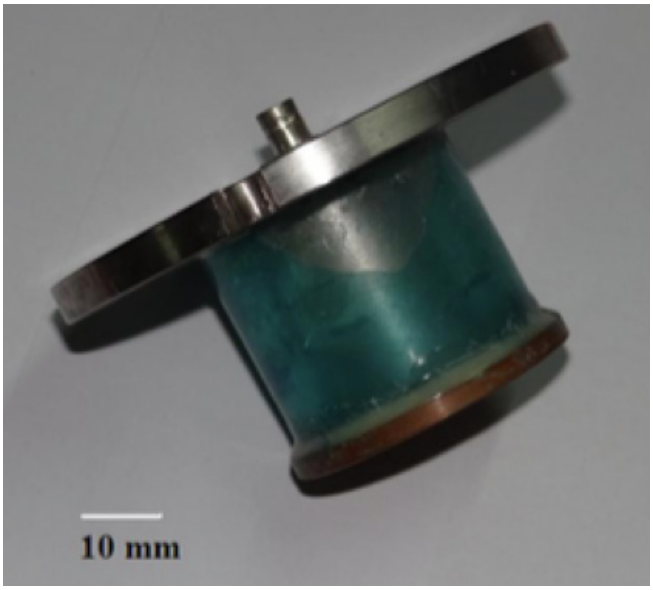

Figure 2-1. Fabricated voltage divider by Mitra [18] capable of measuring sub-nanosecond rise times.

A relatively new method to reduce EMI associated with high voltages is through the use of optical sensors [21,24]. Optically sensing high voltages provides additional advantages over conventional methods by allowing almost perfect isolation between the high voltage system and the measurement device [21]. These optical sensors typically rely on electro-optic effects such as Pockels or Kerr effect to implement optical transducers capable of sensing DC, AC, and pulse voltage signals in the hundreds of kilovolts with theoretical speeds in the GHz range [25,26,27,28,29].

2.2 Optical High Voltage Measurement Devices

Optical devices that are used for measuring high voltage operate using electro-optic materials. These sensors use materials whose refractive index changes with the presence of an

electric field. Eq. (2-1) shows the electro-optic relationship between the index of refraction and the applied electric field,

$$n(E) \approx n + \text{ŕ}E + \text{ś}E^2, \tag{2-1}$$

where n is the refractive index of the material with no electric field present, ŕ represents the linear electro-optic effect on the material which is also known as the Pockels coefficient, and ś is the quadratic electro-optic effect on the material which is also known as the Kerr coefficient [21,30]. Other higher order factors exist within the electro-optic medium [30,31], but they are often many orders of magnitude smaller than n, and thus have a negligible effect.

2.3 Pockels Cell

These types of optical sensors have been commercialized and operate by taking advantage of the Pockels effect. These sensors are constructed using multiple polarizers, a quarter or eighth wave plate, and a method by which the light source is coupled from an optical fiber into an electro-optic material and then coupled back into the optical fiber. Figure 2-2 shows a diagram of one such sensor. Since the Pockels cell is made of and electro-optic birefringent material, an applied voltage creates an electric field that modulates the birefringence of the cell, which in turn modulates the polarization of the transmitted light. A system of polarizers and wave plates can then be used to separate the different polarizations of the resulting light output. While the Pockels sensor is traditionally used for phase or intensity modulation, there have also been cases where they have worked in reverse, where the characteristics of the transmitted light are analyzed to determine the unknown voltage applied to the electrodes of the Pockels cell.

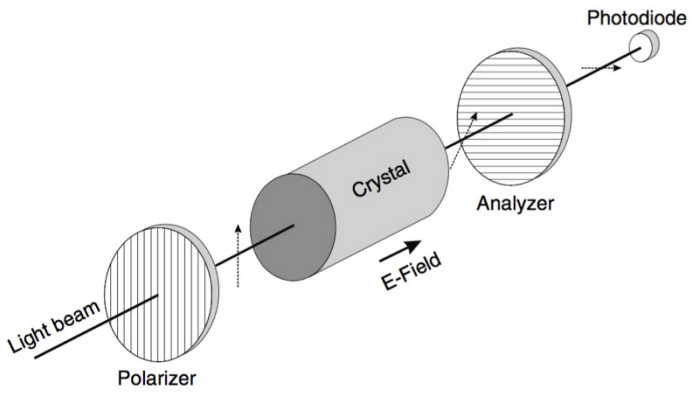

Figure 2-2. Diagram of Pockels Cell, which can be used to measure voltage optically. [20]

Although the Pockels sensor has been developed and is even sold commercially, the polarizers and coupling stages of the sensor often result in optical loss to the system through the sensor.

2.4 SCOS

An alternative way to measure high voltage using optical sensors is through slab-coupled optical sensors (SCOS). SCOS, like the Pockels cell, rely on an electro-optic crystal to measure change in electric field. However, SCOS are composed of fewer components than the Pockels cell, namely a single optical fiber and an electro-optic waveguide. These optical fiber-based electric field sensors are capable of measuring high electric fields and exhibit fast rise times, and their all-dielectric nature allows them to be non-intrusively incorporated into systems [13]. SCOS are also small, having a cross section of about 0.3 mm x 0.2 mm, allowing them to be placed in small spaces [3,4]. SCOS have a relatively simple composition and less coupling connections compared to other optical sensors, as a result SCOS easily avoid additional coupling losses. Additionally, SCOS configurations have been developed to be able to significantly reduce phase noise [5,6] and improve the SNR of the signal [14], even in harsh environments [7,8].

3 SCOS BACKGROUND

SCOS are electric field sensors created using a PM fiber and an electro-optic slab waveguide. These devices utilize the linear electro-optic effect (Pockels effect) as well as evanescent waveguide coupling to detect electric field. Traditionally, D-fibers with an elliptical core were used [32]. However, side-polished Panda fiber has also been used to create SCOS [33,34]. In both instances, the principle is the same: a close proximity between the core of a PM fiber and the crystal waveguide allows for evanescent coupling from fiber to the waveguide. Figure 3-1 shows a cross sectional view of a D-fiber. The slab waveguide (not shown) is attached to the flat side of the fiber.

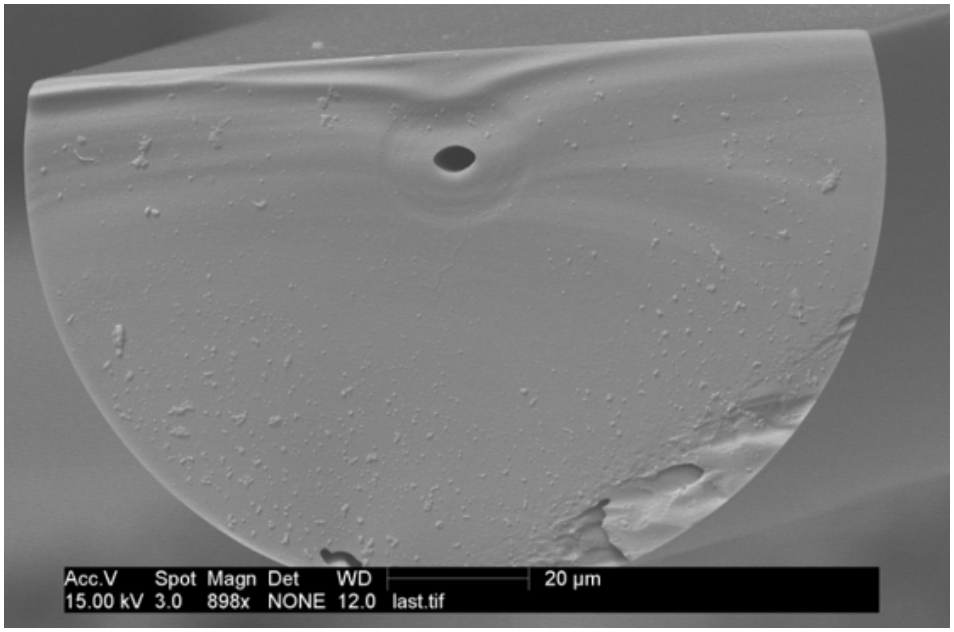

Figure 3-1. Cross-sectional view of D-fiber, which is used in SCOS fabrication.

As light propagates through the fiber, it can couple out of the fiber into the electro-optic crystal slab waveguide. The waveguide used in this work is $LiNbO_3$, but other electro-optic materials can be used such as KTP, $LiTaO_3$, or electro-optic polymer [32,35].

In order for the light to couple out of the fiber via the slab waveguide, the core of the fiber and the slab waveguide must be close enough for evanescent coupling to occur. A short section in the middle of the D-fiber is stripped of its plastic jacket and then etched in hydrofluoric acid. This etches away part of the cladding, which further exposes the evanescent field and allows optical coupling between the core of the fiber and the crystal. A $LiNbO_3$ crystal slab waveguide is placed on top of the flat surface of the D-fiber, and the crystal's close proximity to the core of the fiber allows certain wavelengths of light to couple out through the slab waveguide. Figure 3-2 shows a diagram of an etched section of D-fiber which has an electro-optic waveguide placed upon the flat side of the fiber. When an optical signal propagates through the fiber, the $LiNbO_3$ waveguide couples certain wavelengths of light out of the fiber.

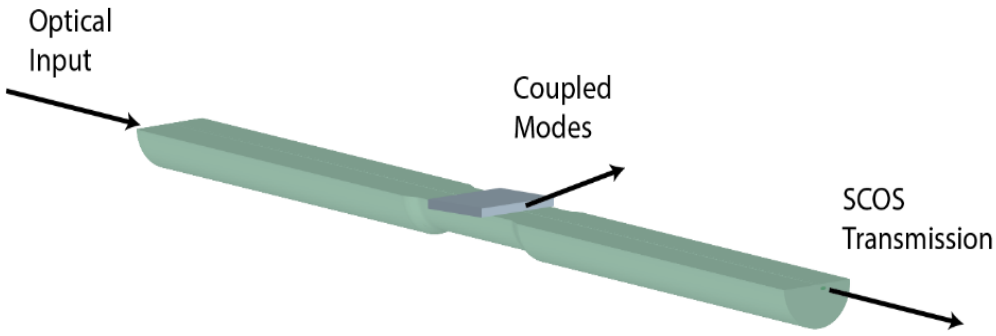

Figure 3-2. An etched D-fiber with an attached electro-optic waveguide. When an optical signal is propagated through the fiber, the $LiNbO_3$ waveguide couples a portion of the light out of the fiber.

Only certain wavelengths of light couple out from the optical fiber via the waveguide. These wavelengths are determined by the geometry and physical parameters of the fiber/waveguide system [36,37], and are given by [38,39,40]

$$\lambda_m = \frac{2t}{m}\sqrt{n_o^2 - N_f^2}\,, \tag{3-1}$$

where λ_m represents the wavelengths that are coupled from the optical fiber into the crystal waveguide, t is the thickness of the slab waveguide, m is the mode number, n_o is the index of the electro-optic crystal waveguide, and N_f is the effective index of refraction of the optical fiber mode.

Due to the wavelengths of light lost through the crystal, the output power spectrum will contain dips, or resonances, at these wavelengths. Figure 3-3 shows an example of a resonance seen from transmitting a broad-spectrum source through a SCOS. In this resonance, the signal reaches maximum attenuation around 1561.4 nm.

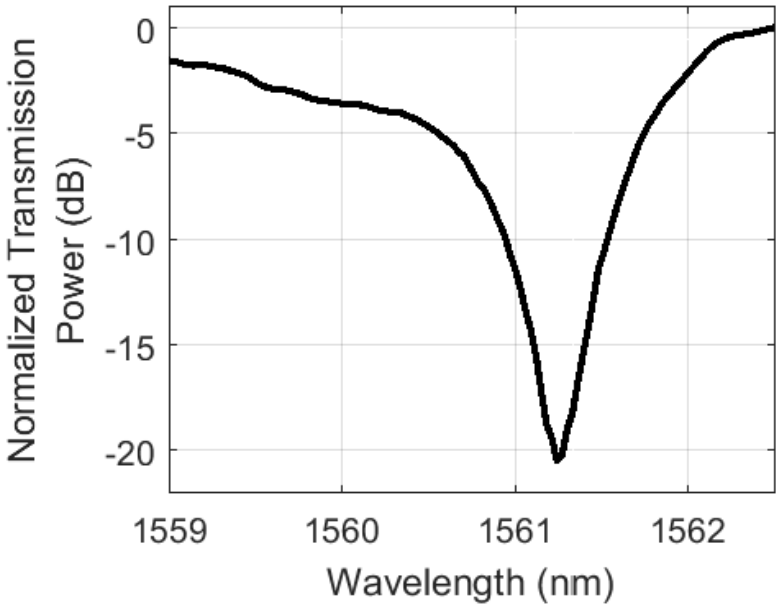

Figure 3-3. Transmission spectrum of a SCOS sensor. The transmission drop occurs due to light coupled into the slab waveguide at certain wavelengths.

The $LiNbO_3$ crystal waveguide is an electro-optic material, which means that it undergoes a change in refractive index when exposed to an electric field. The relationship between the

refractive index and the electric field can be summarized through an electro-optic tensor matrix [32, 41],

$$\begin{bmatrix} 0 & -r_{22} & r_{13} \\ 0 & r_{22} & r_{13} \\ 0 & 0 & r_{33} \\ 0 & r_{51} & 0 \\ r_{51} & 0 & 0 \\ -r_{22} & 0 & 0 \end{bmatrix}, \tag{3-2}$$

where r_{13} = 8.6 pm/V, r_{33} = 31 pm/V, r_{22} = 3.4 pm/V and r_{51} = 28 pm/V. Although this effect will not be explained in detail in this thesis, the equation of interest [30,38,41],

$$\Delta n_o = \frac{1}{2} n_o^3 r_{33} E, \tag{3-3}$$

shows how the index of refraction, n_o, is changed with the presence of an electric field E, where r_{33} is the electro-optic coefficient of the lithium niobate ($LiNbO_3$) crystal in the optic axis direction and E is the electric field applied in the direction of the crystal's optic axis. Eq. (3-1) states that this results in a shift in wavelengths at which resonances appear in the output spectrum. By propagating a laser, which is tuned to the edge of one of these resonances, through the SCOS sensor, the measured output power shifts when the SCOS is influenced by an electric field. By monitoring this power change, the field applied across the SCOS can be deduced. This is done by assuming an approximately linear relationship between E-field and optical power shift for small changes in E-field or by finding the exact relationship through nonlinear correction methods explained in [9,10]. By relating this electric field to the known geometry, the voltage applied across the SCOS can be deduced.

Figure 3-4 (right) shows that as an electric field across the SCOS fluctuates, the spectrum (left) shifts from its original position (dashed) to its new position (blue). Figure 3-4 (left) shows that by aiming a laser at the resonance edge and, as the electric field alternates, we see a

proportional increase and decrease in output power. Therefore by measuring this fluctuation of transmitted optical power, we can deduce the fluctuation in electric field.

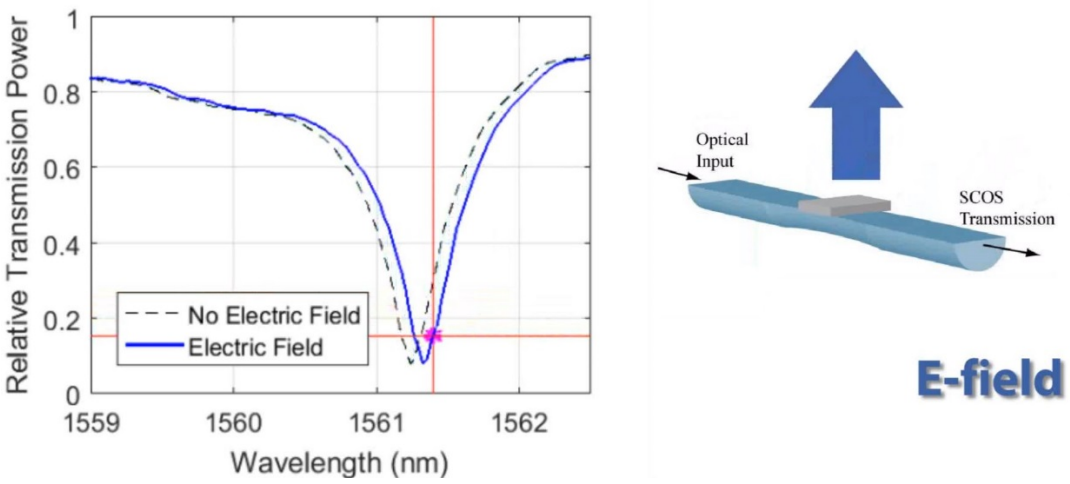

Figure 3-4. As a change in electric field causes a change in the refractive index of the waveguide, the original transmission spectrum (black, dashed) is shifted (blue) proportional to the applied electric field. The laser (in this example tuned to 1561.4nm) propagating through the SCOS sensor transmits an optical power proportional to the shift in applied electric field.

4 ADAPTING SCOS FOR MEASURING HV SYSTEMS

4.1 Issues with High Voltage Systems

Certain precautions need to be taken when dealing with high voltage systems. Some of the issues encountered when attempting to use SCOS in high voltage applications are corona discharging, as well as unwanted arcing and electromagnetic interference (EMI).

4.1.1 Corona

Corona discharge is partial electrical discharge through a fluid medium. As the electric field becomes too large, partial discharge or partial breakdown can occur within the medium. The partial breakdown of the material results in ionization of the molecules, which creates a more conductive path within the medium through which electrical energy can discharge. When the partial discharge is stable, i.e. the medium does not entirely break down and no actual arc occurs, this discharge is commonly referred to as “corona”. When corona occurs, the system loses electrical energy, and often a secondary ionization process known as “photoionization” causes the fluid medium to emit a “glow”, which is typically purple or blue [42].

Since the material breakdown depends on the magnitude of the electric field at that point, corona is often greatest where the electric field is the strongest. Since the magnitude of the electric field is typically greatest on “sharper” edges of a highly-charged surface, these locations often exhibit more prominent corona discharge. To demonstrate this principle, a Van de Graaff

generator is used to generate a high voltage potential on the metal surface. Figure 4-1 shows the surface of this generator, which experiences corona discharge as a finger gets close to the highly-charged surface of the generator. As the finger gets close to the generator, the air becomes ionized between the finger and the generator, and purple spindles are visible between the two objects. These lightning-like spindles show where the air is ionized enough to provide a more conductive pathway for the electrical discharge. The corona is most prominent where the electric field is strongest between the hand and the high voltage potential of the metal sphere of the Van de Graaff generator on the left. In this case, the outstretched finger appears to have the highest localized field, this field is especially localized on the sharp tip of the finger nail. Relatively sharp geometry such as this is more prone to introduce energy losses in the system, especially at higher voltages.

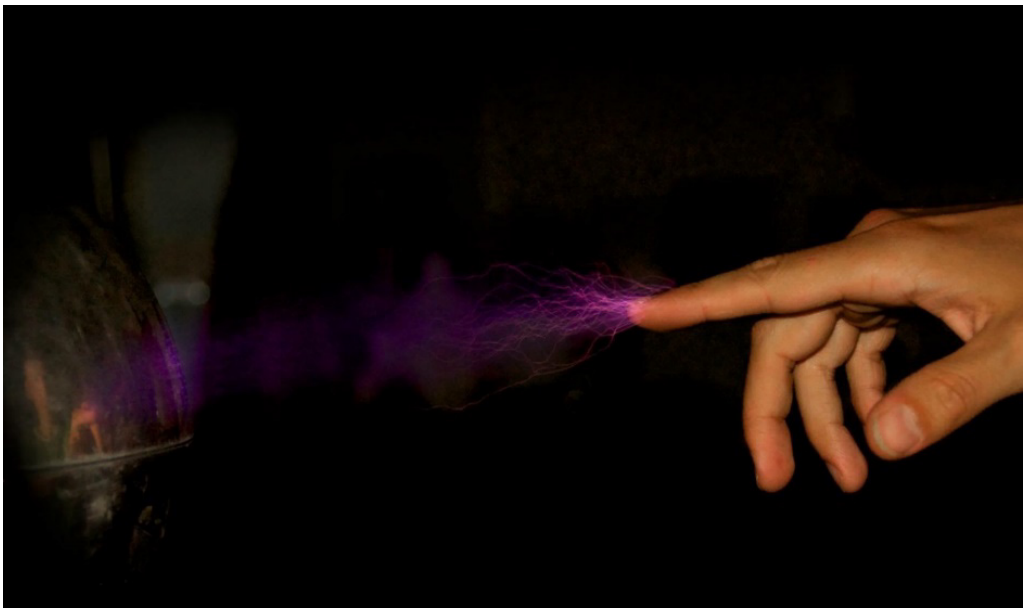

Figure 4-1. Corona discharge appearing as a purplish glow from the electric field produced between a charged Van de Graaff generator and a hand. Spindles of lightning protrude from the finger, showing the ionized conductive air pathways between the generator and the finger.

4.1.2 Unwanted Arcing

While corona discharge describes a stable partial discharge within a medium, arcing describes complete breakdown of the medium. This occurs when the voltage potential reaches a level higher than the breakdown strength of the medium. At this point, the air forms a conductive path where electrical energy can flow freely, allowing most of the electrical energy to be discharge through the arc [43].

4.1.3 Electromagnetic Interference

Arcing is often a very quick pulse with a very fast associated rise time. As the arc discharges the high voltage potential, a high electromagnetic (EM) pulse is often produced. This EM pulse can propagate through space and can induce unwanted electrical currents into the electronics of the system.

The EMI within the system scales with voltage, and since the voltage in high voltage systems are, by definition, much higher than in conventional/traditional low voltage systems, the EMI created by these systems are also larger.

4.2 Preventing Corona Losses and Arcing

The undesirable losses resulting from corona and arcing can be somewhat remedied through the use of gases, oils, and solids with high dielectric strength.

4.2.1 Different Gases

Since corona appears when the medium undergoes dielectric breakdown, increasing the inherent electrical breakdown of the medium can help prevent some of that discharge. Table 4-1 summarizes the electrical breakdown of various gases. Although atmospheric air is the cheapest,

most accessible, and most convenient dielectric gas, it is a relatively poor dielectric compared to other gases such as sulfur hexafluoride (SF_6), Selenium hexafluoride (SeF_6), or Carbon tetrachloride (CCl_4). In practice, SF_6 is the most commonly used gas in HV systems, and extensive scientific research has been done to determine its characteristics and dielectric properties [42].

Table 4-1. Electrical breakdown strength of various gases ranked from smallest to largest [42].

Gas or Vapor	Breakdown Strength (MV/m)
Helium (He)	0.37
Neon (Ne)	0.42
Argon (Ar)	0.65
Hydrogen (H_2)	1.5
Methane (CH_4)	2.1
Carbon dioxide (CO_2)	2.5
Oxygen (O_2)	2.7
Water Vapor (H_2O)	~3.0
Air	3.2
Nitrogen (N_2)	3.3
Tetraflouromethane (CF_4)	3.6
Nitrogen oxide (NO_2)	4.0
Carbon monoxide (CO)	4.2
Chlorine (Cl_2)	5.2
Sulfur dioxide (SO_2)	6.4
Sulfer hexafluoride (SF_6)	8.9
Selenium hexifloride (SeF_6)	14.4
Carbon tetrachloride (CCl_4)	18.0

4.2.2 Transformer Oil

Liquid dielectrics, especially oils, can also be used to decrease corona loss and prevent arcing within the medium. Much is still unknown about fluid dielectric breakdown compared to gas or solid dielectrics [43]. Wadhwa even describes their behavior as being so "erratic" that even two samples of oil taken from the same container do not behave identically [43]. With such variation between samples, scientific reports on dielectric strength can often vary significantly from source to source (see [42,43,44]). Table 4-2 shows a summary of various oils and their dielectric properties as reported by Arora. Of the materials listed, the most commonly used oil is transformer oil. Comparing its electrical breakdown value of 30-50 MV/m to gaseous alternatives found in Table 4-1, transformer oil is a much better electrical insulator.

Table 4-2. Electrical breakdown of various oils [42].

Oil Type	Electrical Breakdown, E_B (MV/m)
Castor Oil	17.5-25
Silicone Oil	30-40
Polyhlorinated Biphenyles (PCB)	25-50
Transformer Oil	35-50

4.2.3 Solid Insulation

Similar to utilizing gases such as SF_6 and liquids such as transformer oil, corona can also be reduced by using solid insulation. Solid insulators often have superior dielectric strength compared to gaseous and liquid dielectrics. These materials could be inorganic such as glass, enamel, or ceramics, as well as organic such as resin, paper, or plastic [42]. Solid insulating materials often have very high dielectric strength, sometimes even higher than liquid or gaseous dielectrics. However, unlike liquid or gaseous dielectrics, damage done to solid materials are often permanent [42].

4.2.4 Conductor Geometry

The geometry of the conductors and electrodes in a system can make a substantial difference on the amount of electrical discharge within a system. To illustrate this principle, a high voltage is applied to various electrode geometries. Figure 4-2, Figure 4-3, Figure 4-4 shows these electrodes with the lab lights on and no visible discharge and also with the lights off, so that the corona discharge can be visibly seen.

Figure 4-2 shows an example of an electrode structure that has sharp edges and corners. In the dark (Figure 4-2b) shows that there is significant corona discharge, which is localized on the sharp corners and edges of the electrode. These corona discharges are an electrical loss to the HV system.

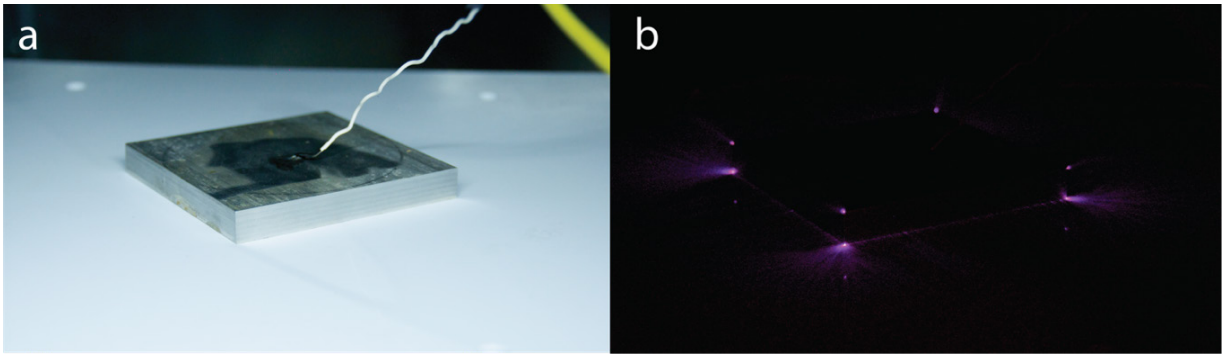

Figure 4-2. Square electrode geometry with a high voltage applied in (a) room light and (b) in the dark.

In general, smoother, rounder electrode geometries help alleviate some of the corona losses. Smoother, rounder surfaces prevent localized electric fields from becoming large enough to result in significant energy loss through corona. Figure 4-3 shows an example of an electrode structure which has slightly less prominent edges than those of the square. It should also be noted that the image exposure is increased to better observe the location of the corona discharge.

Although this disk geometry shows less prominent corona discharge, it is evident that the edges of the disk are still the main contributor to the corona loss.

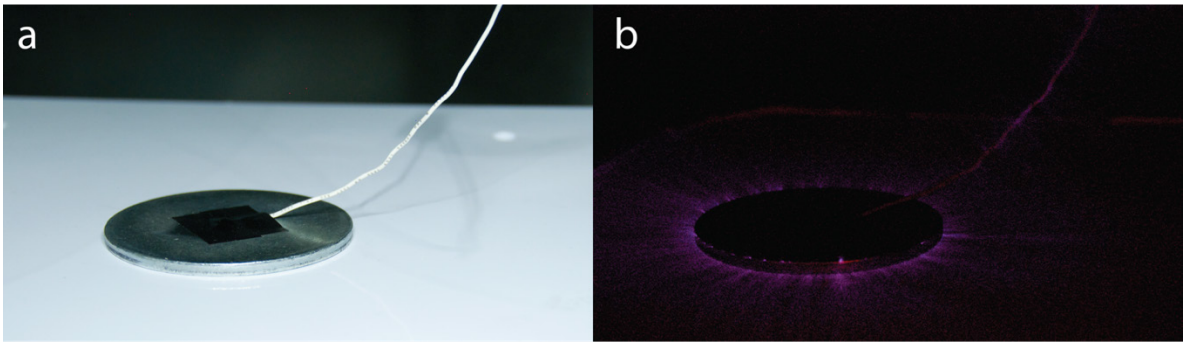

Figure 4-3. Round disk electrode geometry with a high voltage applied in (a) room light and (b) in the dark.

Improving the electrode geometry even further, we can see that eliminating abrupt edges, such as those found in Figure 4-2 or Figure 4-3, significantly reduces the corona discharge. This electrode structure is more of a 'donut' shape, with very rounded edges. Figure 4-4 shows this donut-shaped electrode structure, which is precision-machined to help eliminate highly localized electric field, and thus helps reduce energy lost due to corona. Although there are still corona losses, these losses are minimized by improving the shape of the electrode.

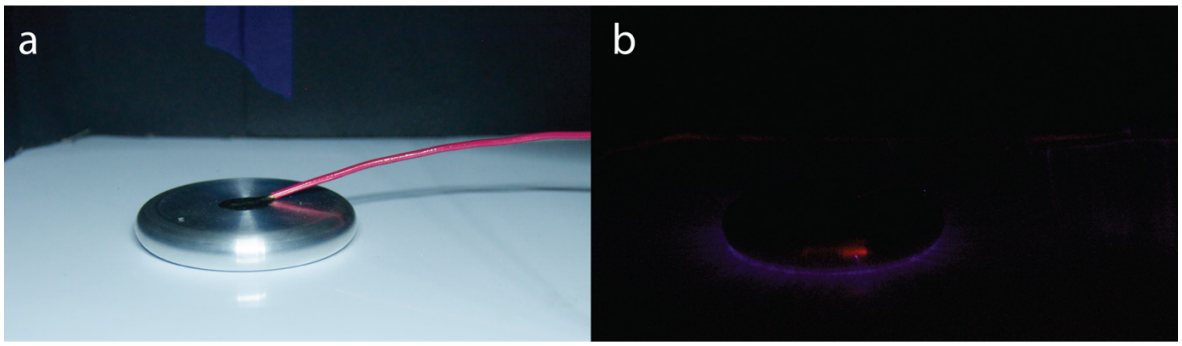

Figure 4-4. An improved electrode structure that has smooth, round edges to minimize corona discharge.

4.3 Minimizing EMI

As stated in Section 4.1.3, high voltage pulsed systems create undesirable EMI. This EMI can affect electronics and introduce large amounts of noise into measurements.

These interferences, which can be induced on wires and electronic circuits, are a problem in measurement accuracy. An EMI test done in the laboratory demonstrates some effects on measurements. The measurement setup consists of a long coaxial cable coiled up with one end connected to the input of a variable gain TIA, and the other end left open. The TIA has a saturation voltage of 4 V, meaning that any output larger than 4 V is automatically clipped. The output of the TIA is then connected to an oscilloscope. This measurement setup is placed in room 1 of a brick building while a HV arc generator is placed in room 3. The wooden doors are closed, and a HV electrical arc is produced in room 3 as the oscilloscope setup records measurements.

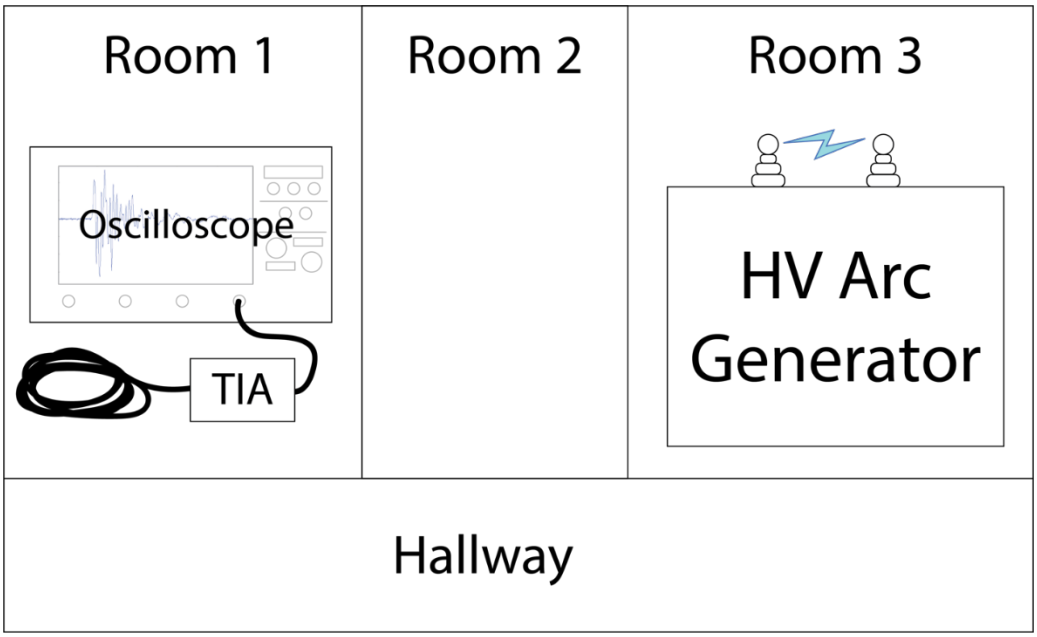

Figure 4-5. Layout of equipment during an EMI test in the lab. A HV arc is produced in a closed room while the oscilloscope, TIA, and coiled up coaxial cable picks up the signal from 2 rooms away in room 1.

Ideally, the spectrum recorded on the oscilloscope would be unaffected by the outside noise emitted by the HV arc generator placed a couple rooms down the hall. However, because the high voltage, fast discharge arc generator produces so much EMI, this discharge affects the measurement setup in room 1. Figure 4-6 shows the spectrum recorded during the HV arc generator discharge by the oscilloscope in the setup shown in Figure 4-5. Even though one of the ends of the coiled-up coaxial cable is left open, the oscilloscope picks up a very large signal ranging from -34 V to 27 V due to the EMI emitted from the HV arc. Also, the sheer magnitude of the signal suggests that the signal is not merely an amplified output from the TIA since the TIA clips its output at 4 V. It can be concluded that the EMI in the HV arc discharge circuits is so disruptive to measurements that steps need to be taken to minimize these effects.

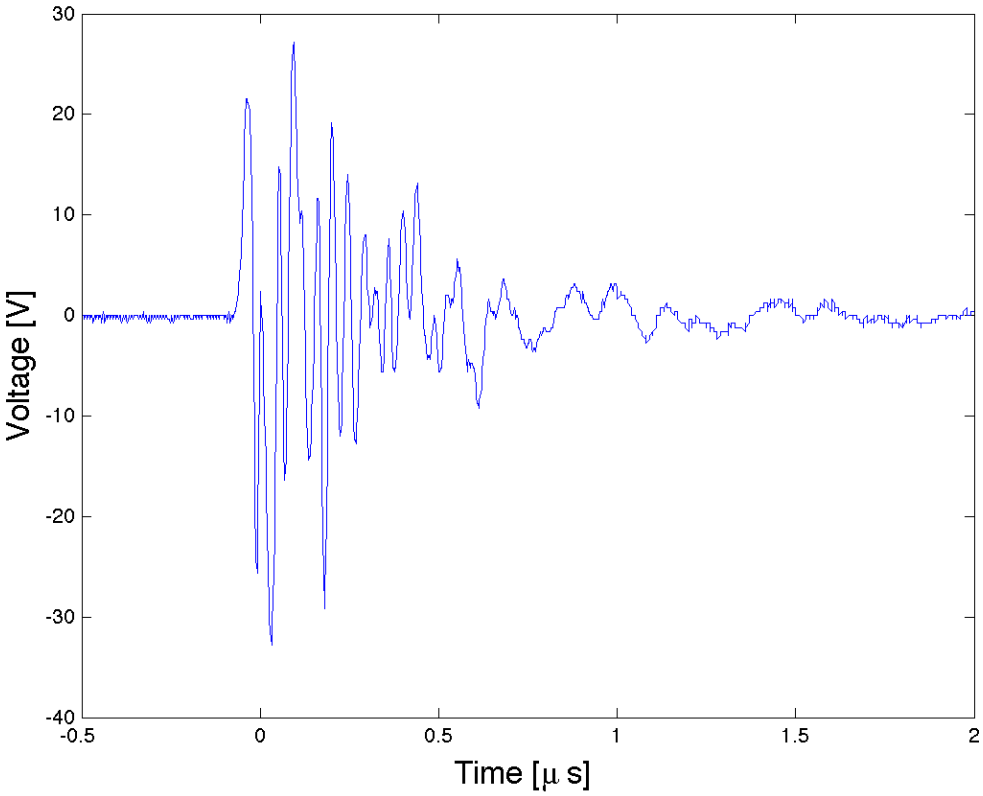

Figure 4-6. EMI recorded on the oscilloscope using the setup shown in Figure 4-5.

4.3.1 Using Faraday Cages

A Faraday cage is an enclosure that is designed to block EMI. These enclosures have been used extensively in research and EM testing and experimentation. These Faraday cages provide one of the most effective methods to eliminate EMI in system measurements. BYU's Faraday cage is showcased in this section.

Figure 4-7 shows the outside of the Faraday cage at BYU. The walls are made with sheet metal, and the "windows" are constructed using a fine copper mesh, which allows for light to pass through, but blocks RF frequency EM.

Figure 4-7. Outside of the Faraday cage at BYU.

Figure 4-8 Shows the inside of the Faraday cage, which is spacious enough (12.4 m^2) that a test setup can be comfortably set up inside. The light from outside can illuminate the workspace through the windows, while RF is blocked.

Figure 4-8. Inside view of the Faraday cage at BYU. A HV test setup such as this can be setup inside, and the double layered fine metallic mesh on the windows allows for natural light to reach the experimental setup but limits RF frequency penetration.

Figure 4-9 shows the coupling connections and access holes on the inside of the Faraday cage. A test setup can be placed inside the Faraday cage while the measurement equipment can be placed outside of the Faraday cage. These holes provide a means by which the inside of the

Faraday cage can be accessed via cable connection from the outside when the doors to the Faraday cage are closed.

Figure 4-9. Inside view of the coupling connections on BYU's Faraday cage.

Figure 4-10 shows the coupling connections in Figure 4-9 on the outside of the Faraday cage. Brass caps can be fastened on the access holes when they are not in use to limit the amount of EMI allowed to escape the Faraday cage.

Figure 4-10. Outside view of coupling connections on BYU's Faraday cage.

Figure 4-11 shows the door to the Faraday cage which can be closed during testing. Like the walls, the door of the Faraday cage is constructed of sheet metal and grounded with the rest of the Faraday cage. Extra care is taken on the door to create an EMI-secure seal along the edges of the door. The seal on the door is so tight that significant force must be applied to the door handle until the door fits snug against the door frame.

Figure 4-11. A metallic door offers access to the Faraday cage, but can be secured against RF penetration upon closure.

The system was tested using the Faraday cage at BYU after EMI and measurement distortions were manifest from testing high voltage arc discharges (Figure 4-5 and Figure 4-6). The RF isolation provided by the Faraday cage allowed for significantly cleaner measurements that were less prone to EMI generated by the HV arc.

4.3.2 Optical Measurements

One of the biggest advantages to using SCOS for HV measurements is that the SCOS is made entirely of dielectric material. Since conductive cables are more susceptible to induced current and EMI, using them in HV, fast discharge systems can often produce noisy and inaccurate measurements. Using optical measurement techniques reduces the effects of unwanted EMI on the measurement system. Additionally, using fiber optic cables in place of conductive cables allows electrical separation between the measurement system and the high voltage system. This greatly mitigates the risk of high voltage arcing through the cables, preventing equipment damage and/or human injury.

Figure 4-12 shows how an optical setup can be used in conjunction with a Faraday cage, so that the HV system can be measured with minimal EMI affecting the measurements. The high voltage system is placed within the Faraday cage, ensuring minimal EMI from the HV system. SCOS are used to measure the output of the HV setup, and the SCOS setup is supported via optical fiber. The optical fiber runs between the HV setup inside the Faraday cage and the measurement setup outside of the Faraday cage via the access holes shown in Figure 4-9 and Figure 4-10. All electrical measurement equipment and cable connections can therefore be placed a safe distance from the HV setup resulting in measurements that are less susceptible to EMI.

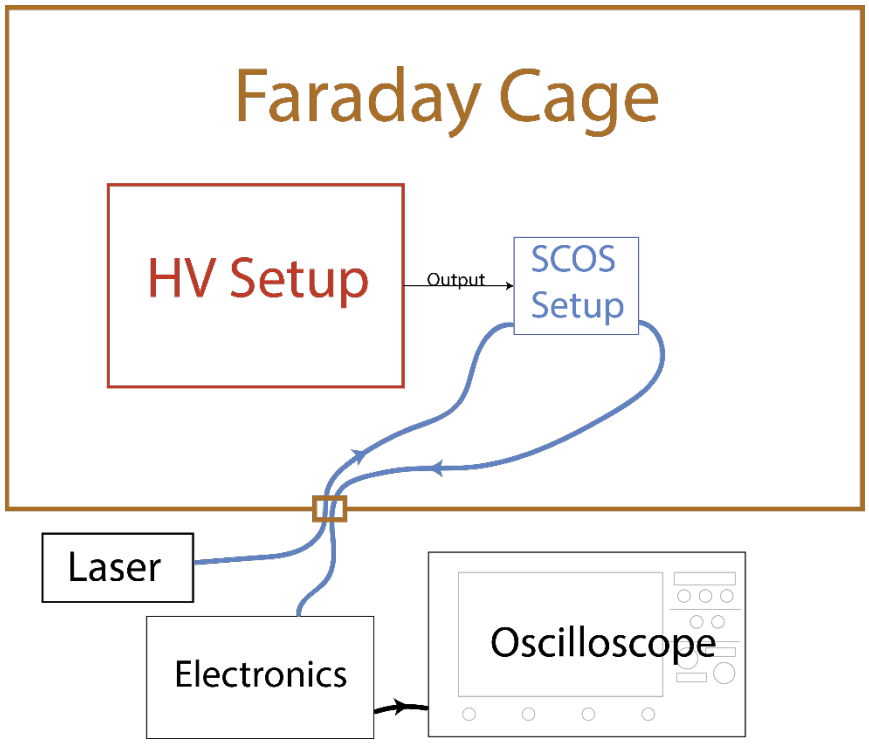

Figure 4-12. Optical connections (in blue) are used between the experiment setup and the measurement setup within a Faraday cage, which helps reduce EMI induced on wires and conductive cables (such as the black line).

4.4 Using an Electrode Structure/Calibration

Although SCOS sensors are only sensitive to electric fields, voltage can be measured using SCOS by converting the voltage in question to an electric field. This is done by connecting the voltage to a known electrode geometry. By taking two parallel metal plates, setting them a set distance apart from each other, and placing a SCOS between them, the electric field between the plates is given by

$$E = \frac{V}{d}, \tag{4-1}$$

where E is the resulting E-field when a voltage V is applied across two parallel plates placed d meters apart. Therefore, a linear increase in voltage corresponds to a linear increase in electric field. Figure 4-13 shows the electrode structure used in taking SCOS measurements. This

structure consists of two copper plates, measuring 120 mm x 100 mm each. The acrylic base of the structure determines the spacing of the copper plate electrodes, and this spacing can adjust to accommodate smaller spacing for lower voltages as well as larger spacing for higher voltages. The SCOS is placed within the electrode structure, between the parallel plates. As the high voltage output of a device connects to the electrode structure via the 2 lead wires ('+HV' and 'GND'), the SCOS is able to measure the voltage.

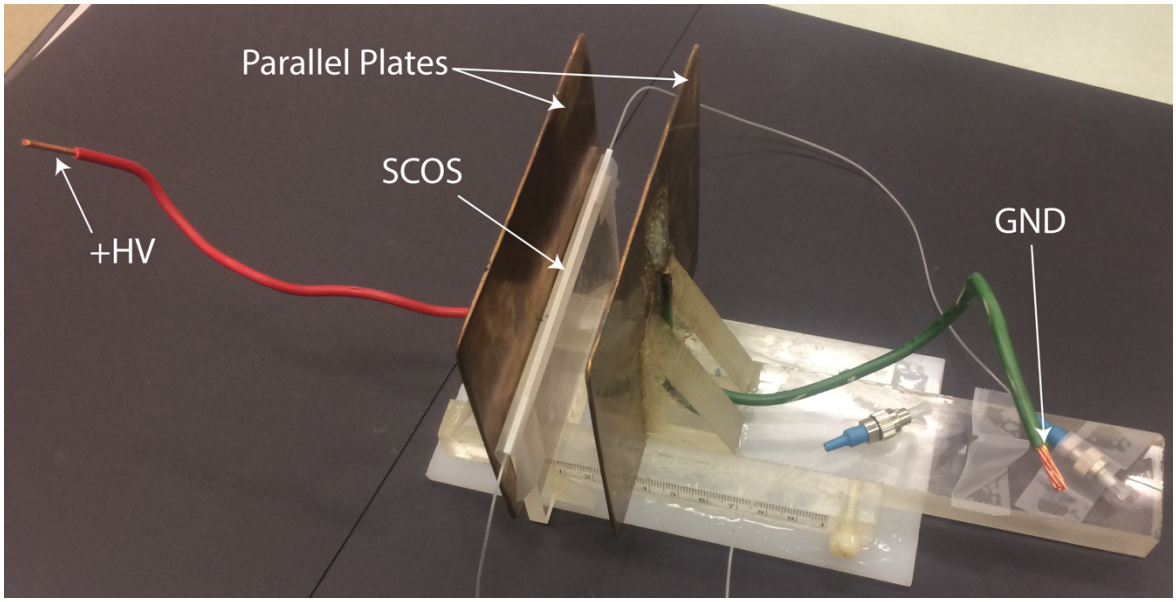

Figure 4-13. Electrode structure used in SCOS measurements, where the SCOS is placed inside the structure and the high voltage connects across the +HV and GND lead wires.

Figure 4-14 shows that the basic setup consists of a parallel plate electrode, which converts the voltage into an electric field. A tunable laser that is transmitted through the SCOS is modulated via the electric field applied across the SCOS. This modulated optical signal from the SCOS is then converted to a current via a photodiode (PD) and then converted to a measurable voltage using a trans-impedance amplifier (TIA). The resulting voltage is then measured by an oscilloscope.

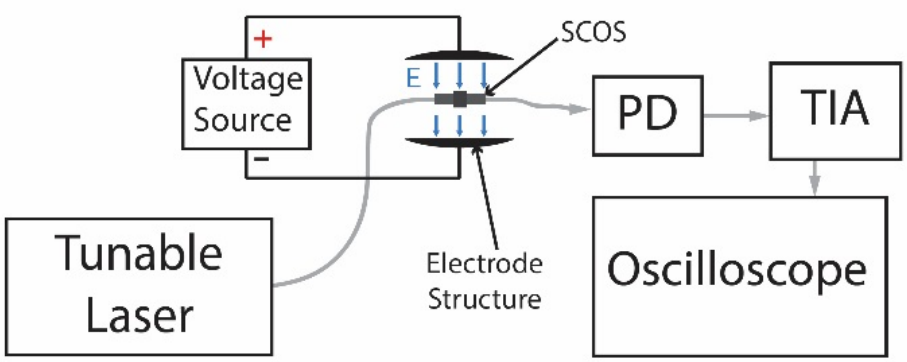

Figure 4-14. Optical setup for converting an electric field into a measurable voltage signal using SCOS technology.

By applying a known voltage across the plates, the magnitude of the resulting signal is recorded. From the calibration results, a 'calibration factor' is obtained that relates the voltage seen by the oscilloscope to the actual voltage applied to the parallel plate structure.

Figure 4-15 shows that SCOS voltage spectrum is recorded on the oscilloscope as the 6 kVpp signal is applied across the electrodes.

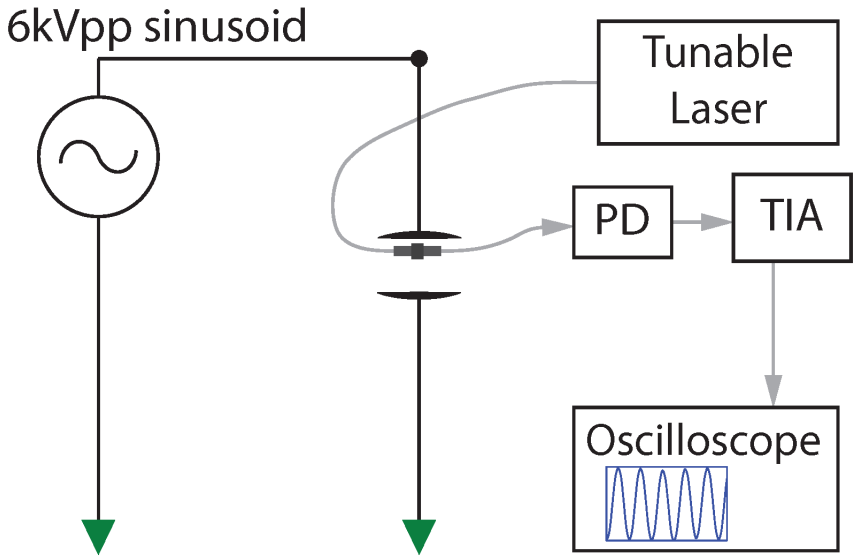

Figure 4-15. A known 6 kVpp voltage source is connected to the setup shown in Figure 4-14, resulting in a similar spectrum on the oscilloscope.

The voltage on the oscilloscope is associated with the actual voltage applied to the electrode structure via a calibration factor. Figure 4-16 shows that the SCOS voltage is measured to be 196 mV when a 6 kVpp voltage is applied to the parallel plate electrode. The oscilloscope shows the voltage (blue), which directly corresponds to the actual voltage applied to the electrode structure (green). Knowing that the 0.196 Vpp voltage signal captured by the oscilloscope corresponds to a voltage of 6000 Vpp applied to the electrode structure, we can calculate a calibration factor to be C=6000/0.196=30.6 kV/V.

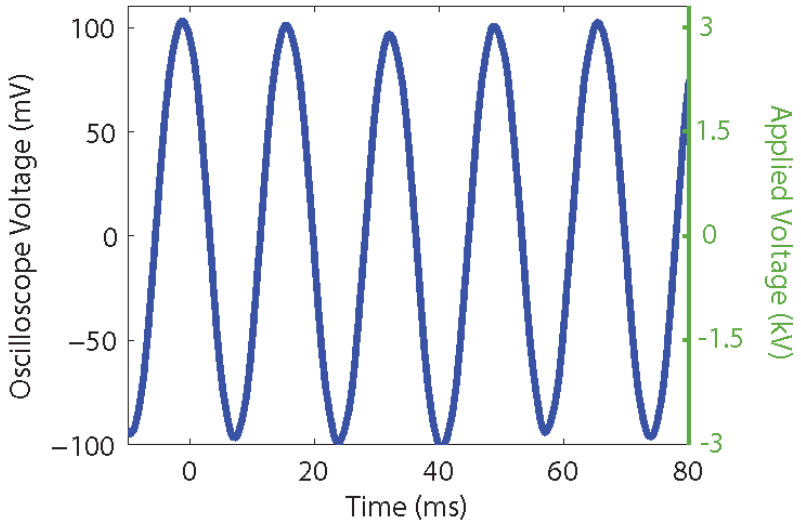

Figure 4-16. The magnitude of the voltage signal recorded by the oscilloscope directly corresponds with the actual voltage applied across the electrode structure.

After the calibration factor is obtained, the 6 kVpp calibration voltage source is replaced with the voltage to be measured. As long as the geometry of the parallel plate electrode structure remains unchanged and the SCOS is unmoved, all other subsequent voltages applied to the electrode structure result in a proportional electric field seen by the SCOS sensor, allowing all other measurements to be characterized using the known calibration factor obtained previously

5 COMPARING TRADITIONAL RESISTIVE VOLTAGE DIVIDER MEASUREMENTS AND SCOS MEASUREMENTS

Voltage dividers are one of the most common ways of measuring voltage. Some of these methods include capacitive dividers, capacitive-resistive dividers, and resistor dividers [45,46]. The resistive divider, in particular, is of special significance due to its relative simplicity.

Although a simple resistive divider can be fairly accurate for low voltages or for lower frequencies, problems may arise when measuring both high voltage and high frequency voltage signals. Although some of the problems associated with high frequencies and voltage divider inaccuracies has been mitigated using more complex voltage divider structures [16,18], simple resistive voltage dividers often introduce distortion and inaccuracies when measuring high voltage AC signals.

This section seeks to illustrate some of the issues associated with using a simple resistive voltage divider and shows some advantages of using SCOS. A SCOS and parallel plate structure were used to measure a high voltage capacitor charge/arc discharge, and these measurements are then compared to similar measurements done using a simple resistive voltage divider.

5.1 HV Ignition Coil Circuit

To show that the SCOS can be used to characterize voltage signals of other systems, a HV charging/discharging circuit is created using an automotive ignition coil. This circuit is then measured using a SCOS and a simple resistive voltage divider.

5.1.1 Basic Operation

A high amplitude, periodic voltage signal was created using a modified automotive ignition coil circuit. Figure 5-1 shows the circuit, which consists of a 12 V car battery, a function generator, an IRF840 MOSFET, and an automotive ignition coil. The transistor acts as a switch and its gate is attached to a function generator outputting an 8 Vpp square wave at a frequency of 175 Hz with a 50% duty cycle. As the transistor switches on and off, the primary of the ignition coil experiences a high change in current, which then induces a voltage on the primary and an even higher voltage on the secondary. This system results in a periodic high voltage output. This output voltage signal is repeated at a rate of 175 Hz as controlled by the function generator.

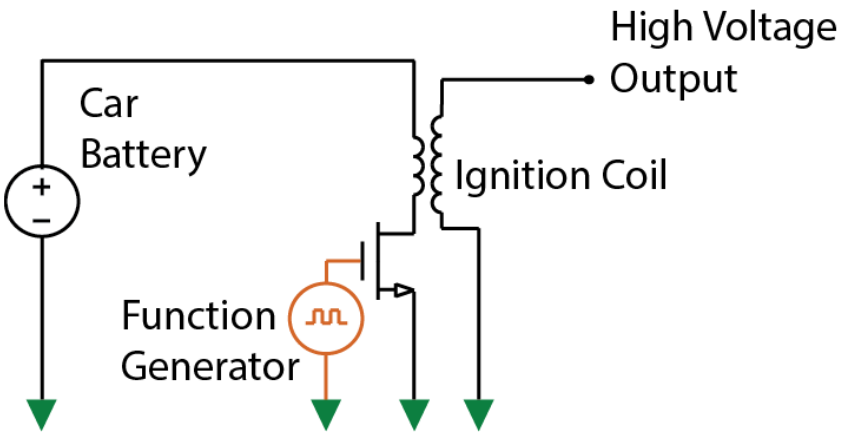

Figure 5-1. Simple high voltage system using an automotive ignition coil transformer. A car battery feeds into the primary coil of the ignition coil and supplies current through the ignition coil and MOSFET. The function generator turns the MOSFET on and off. When current runs through the primary coil, a high voltage is induced, which generates a higher voltage in the secondary and produces a periodic, high voltage output.

5.2 SCOS Measurement Setup

The ignition coil circuit in Figure 5-1 acts as the input to a simple capacitor charge/ discharge circuit. Figure 5-2 shows this charge/discharge circuit, which has a HV diode placed in series with the ignition coil circuit and charges a 2 nF capacitor to the peak value of the "ignition coil setup" circuit. As the ignition coil circuit supplies a periodic high voltage through the diode, the voltage on the capacitor increases with the periodicity of the ignition coil circuit, which is set to 175 Hz (every 5.7 ms). To periodically discharge the capacitor, a wire spark gap is used. Once the voltage on the capacitor exceeds the breakdown voltage of the wire spark gap, the spark gap arcs, discharging the voltage on capacitor. As the circuit operates, the SCOS setup with the electrode structure outlined in Section 4.4 measures the voltage on the capacitor.

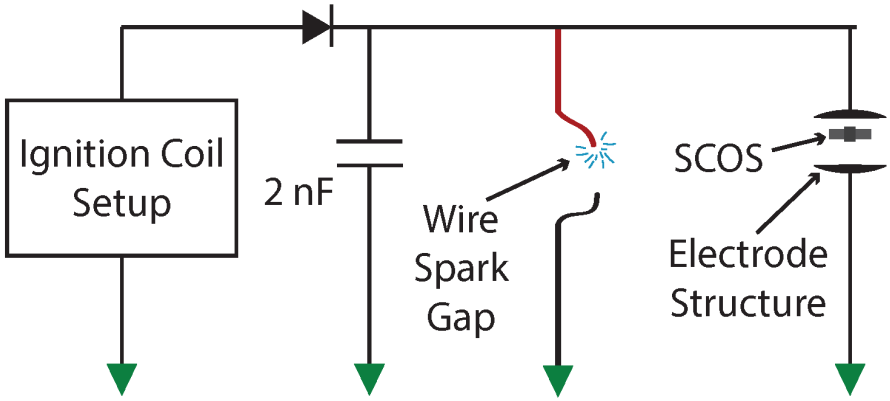

Figure 5-2. Capacitor charging/discharging circuit measured using a SCOS.

5.3 SCOS Measurements

As the electrode structure contains the SCOS, the SCOS measures the voltage on the capacitor of the setup in Figure 5-2. Figure 5-3 shows that the voltage on the capacitor increases periodically every 5.7 ms, which corresponds to the 175 Hz frequency of the charging circuit. The ignition coil charging circuit periodically adds to the voltage on the capacitor until the

voltage is large enough to arc between the spark gap. Once the spark gap arcs, the capacitor discharges via the arcing. The charging/discharging sequence is then repeated.

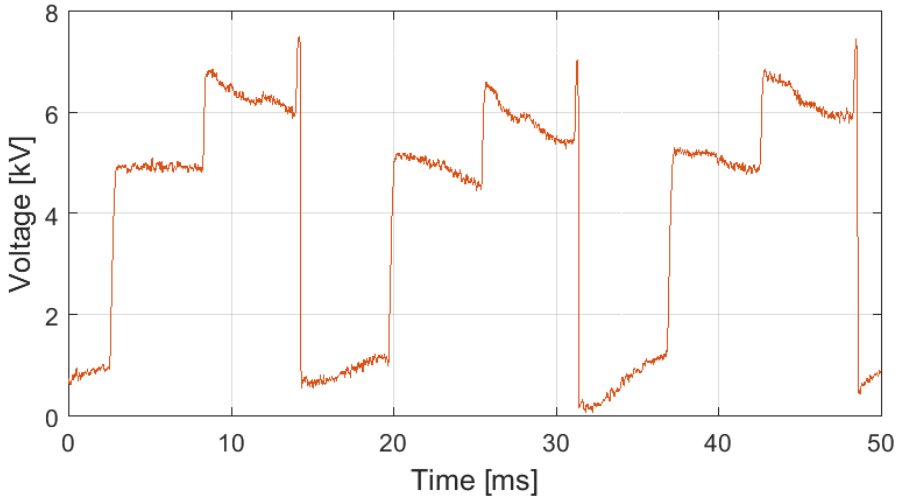

Figure 5-3. The voltage on the capacitor as measured by the SCOS sensor. The capacitor's voltage increases periodically in voltage until the voltage is high enough to arc across the spark gap.

To illustrate the dynamics of the circuit shown in Figure 5-2, Figure 5-4 shows a progression of screenshots of the spark gap as well as the corresponding voltage on the capacitor. These screenshots were taken from a video using a Casio EX-ZR800 digital camera recording at a framerate of 1000 fps. Like measurements shown in Figure 5-3, the voltage across the capacitor increases periodically as a rate of 175 Hz (Figure 5-4a, Figure 5-4b, and Figure 5-4c). Since the voltage on the capacitor is the same as the voltage across the spark gap, it eventually reaches an amplitude that is greater than the breakdown of air between the spark gap wires. At this point (at roughly 7 kV in this experiment), arcing occurs between the spark gap wires. Using the SCOS, the voltage across the spark gap and across the capacitor are dynamically measured. Because the SCOS is an all-dielectric sensor, the sensor is less prone to measurement error caused by stray currents and EMI interference [21] from the spark gap.

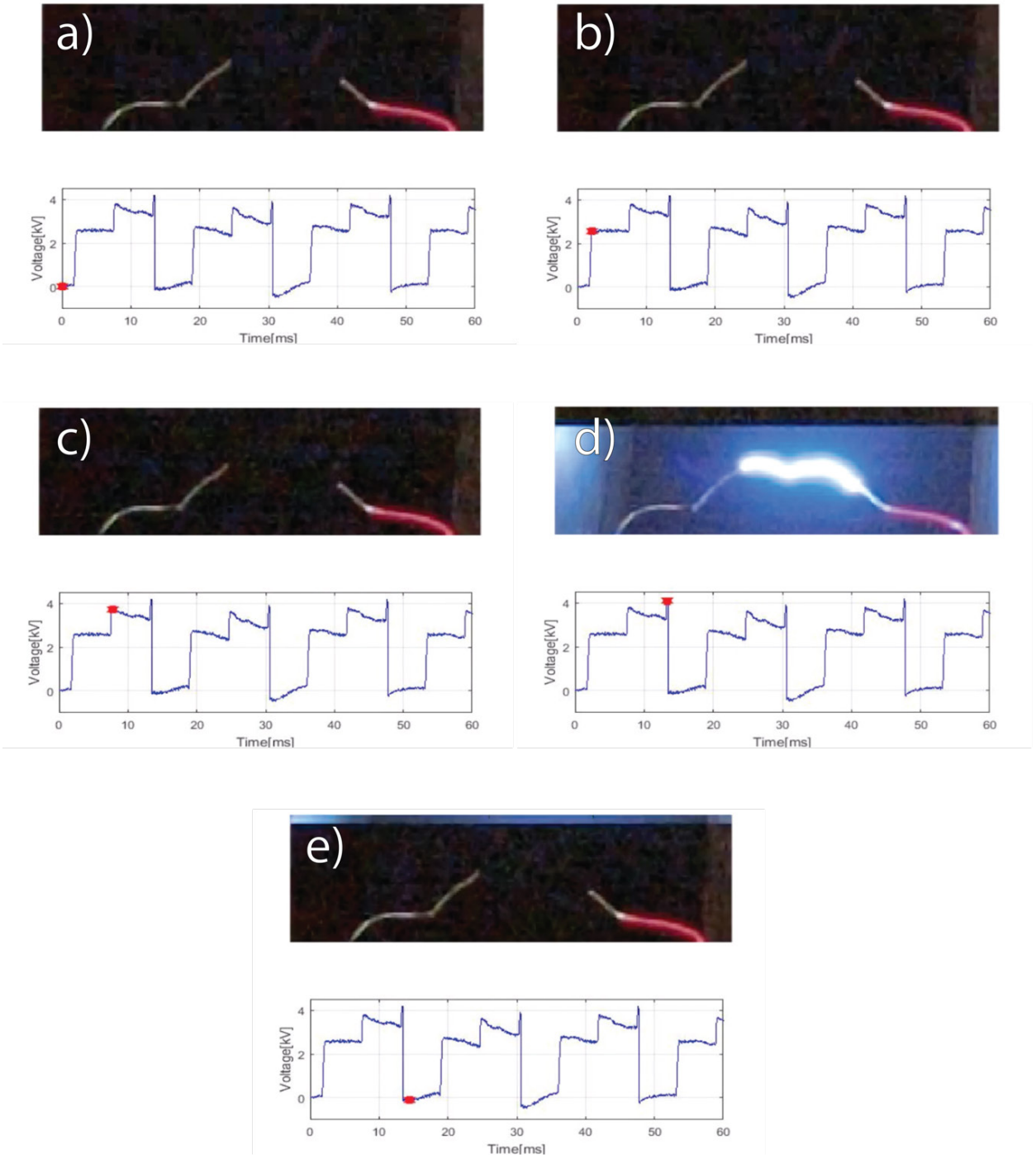

Figure 5-4. Frames taken from a 1,000-fps camera which show the spark gap (silver and red wires) along with the corresponding voltage of the capacitor. The capacitor collects charge periodically (a-c) until the voltage on the capacitor is large enough to exceed the breakdown of air between the spark gap (d). This arc discharges the capacitor almost completely (e).

5.4 Voltage Divider Measurements

Figure 5-5 shows the setup with a resistive voltage divider added. As the voltage divider takes measurements, the SCOS and the electrode structure also measure the voltage on the capacitor. Measurements from the voltage divider are measured while the voltage divider is attached and unattached to the capacitor. (A switch in Figure 5-5 indicates this attaching and detaching of the resistive voltage divider.) The voltage divider is a construction of three 1 GΩ resistors in series with a 330 kΩ resistor. Fortunately, the resistance of the voltage divider offers a large enough resistive load so as to not affect the voltage on the capacitor and the SCOS measurements.

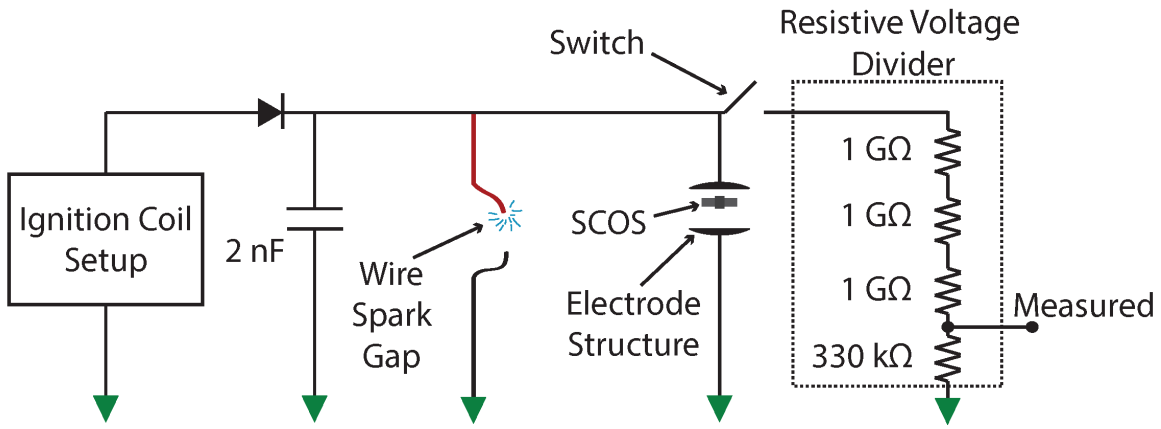

Figure 5-5. 2 nF capacitor charging setup measured using both a SCOS and a resistive voltage divider.

As the square wave is continually applied by the function generator, both the SCOS as well as with the connected traditional resistive voltage divider measure the voltage on the capacitor in Figure 5-5. Figure 5-6 shows these measurements as well as a measurement from the voltage divider when not connected to the circuit (switch disconnected). The SCOS measurement (A) is as predicted, with the capacitor gathering charge every 5.7 ms (175 Hz) until the voltage across the electrodes is high enough to arc across the electrodes and discharge the

capacitor. This arcing corresponds to the sharp downward spike in waveform 'A' occurring around 15 ms, 32 ms, and 48 ms.

The voltage divider measurement with the switch open (B) is noise on the voltage divider caused by the EMI produced from the high voltage circuit. It has fluctuations that correspond mostly to the rising and falling edges of the SCOS measurement.

The voltage divider measurement with the switch closed (C) has a high negative DC component and shows a gradual increase in voltage until the voltage is discharged. The voltage divider measures this discharge as a gradual downward slope rather than a sharp falloff. This voltage divider measurement almost appears as a low-pass filtered version of the SCOS measurement with the added resistor divider noise (B) superimposed on top of the signal.

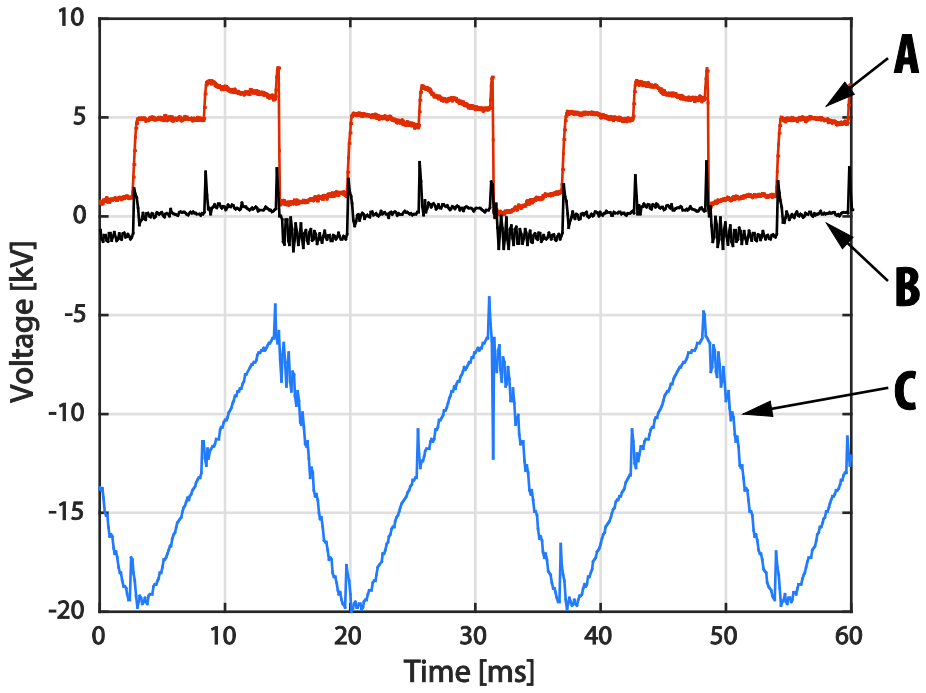

Figure 5-6. Charging circuit measurements with (A) SCOS and the resistive divider with the switch (B) open and (C) closed.

From the measurements shown in Figure 5-6, it is clear that the voltage divider is unable to appropriately capture the dynamic voltage on the capacitor. When the voltage divider is connected (C), the waveform seems almost sinusoidal and has a negative DC voltage offset, both of which do not accurately describe the dynamics of the system. When the voltage divider is completely detached from the circuit (B), the voltage divider's inability to capture the appropriate voltage is even more apparent. Since it is detached from the circuit entirely, the voltage divider would ideally read '0 V' for the duration of the measurement. However, the fact that the voltage divider picks up large voltage spikes indicates that the resistive voltage divider is susceptible to large inaccuracies during dynamic high voltage tests such as these.

5.5 Further Exploration of Voltage Dividers and High Voltage Measurements

In addition to the inaccuracies portrayed in Figure 5-6, common resistor dividers are susceptible to inaccurate measurements of other high voltage, high frequency systems. To illustrate some of these inaccuracies, we use the voltage divider from Figure 5-5 in the setup shown in Figure 5-7. This setup utilizes an HP 33120A function generator, which feeds a sinusoidal signal of 20 Vpp to a Trek 2205 high voltage amplifier. The amplifier increases the input signal by a factor of 50, outputting a voltage of 1 kVpp across the voltage divider. For convenience and monitoring purposes, the high voltage amplifier also supplies a "voltage monitor" output, which is a signal output mirroring the output signal but attenuated by a factor of 50. The setup uses an Agilent DSO3102A oscilloscope to measure two signals on two separate channels. The first is dedicated to the voltage monitor output, while the second is the signal seen by the voltage divider.

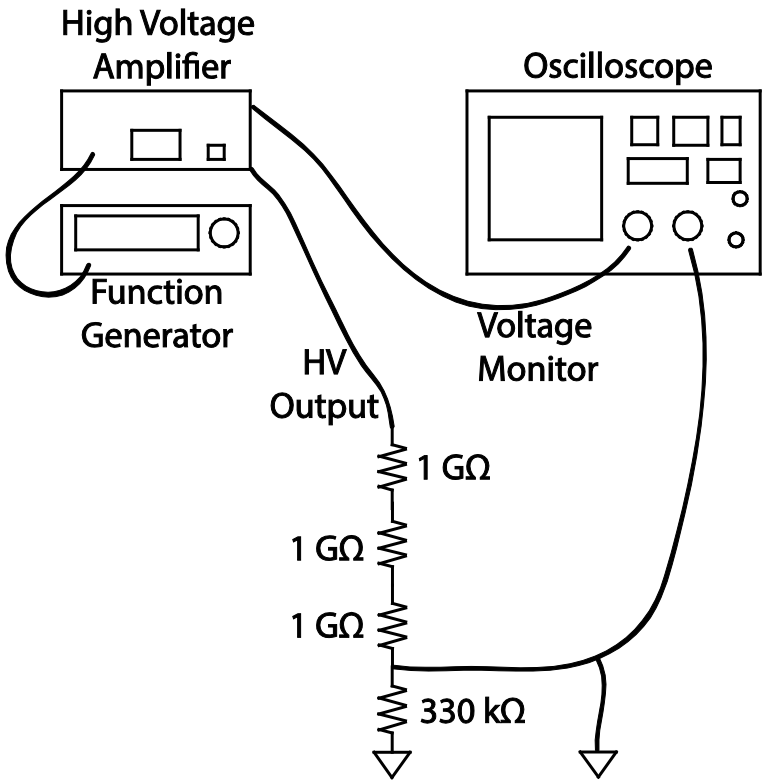

Figure 5-7. Voltage divider setup which compares the mirrored output with that seen by the resistor voltage divider.

Various frequencies serve as inputs to the high voltage amplifier, and the values provided by the voltage monitor, as well as those measured using the voltage divider, are recorded. The voltage divider would ideally be able to obtain the same results as the voltage monitor. However, there are clearly discrepancies, showing that the measurements reflected on the resistor divider are frequency dependent. Figure 5-8 shows these measurements. The expected measurement (dashed line) stays fairly constant at 1 kVpp across frequencies up to 10 kHz, only deviating at most by about 1 percent. The voltage divider measurement of the same signal (solid line), however, deviates by more than a factor of 15 in some instances. This indicates that resistor voltage dividers are not always reliable for some high voltage AC signals.

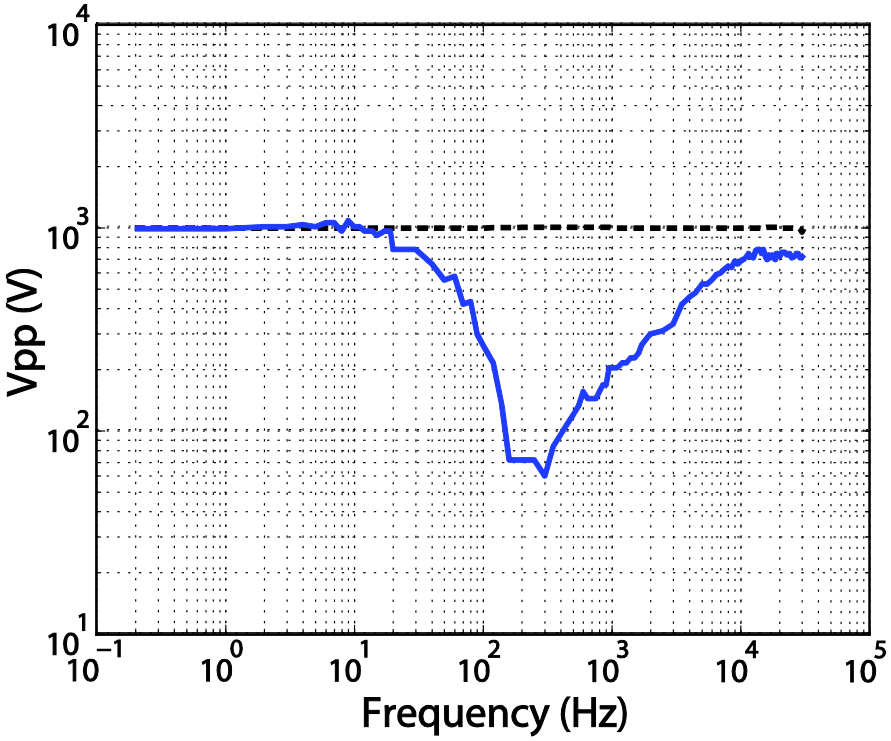

Figure 5-8. This frequency sweep of a 1 kVpp signal shows discrepancy between (dashed) the voltage monitor signal and (solid) the resistor divider.

5.6 Conclusion

Simple resistive voltage dividers are a common method of measuring voltage. However, the common voltage divider often encounters difficulty in measuring some signals, particularly those of high amplitude and high frequency. Using an ignition coil-based high voltage generator, we measured a capacitor's charge and discharge using both a resistive voltage divider and a slab coupled optical sensor. While the voltage divider had difficulty characterizing the waveform, the SCOS is able to measure the step-wise waveform. SCOS offer another means by which voltage signals can be measured accurately and reliably. SCOS could also be a useful tool in analyzing the arc dynamics of a certain circuit [12].

6 USING SCOS TO MEASURE OTHER HV SYSTEMS

In order to truly showcase the ability of the SCOS to measure high voltage systems, SCOS were used to measure the outputs of several high voltage generators. These systems include the ignition coil circuit (used in Section 0), a Marx generator circuit, and a 200 kV capacitor charging/discharging circuit. While the designs and operations vary widely between the three high voltage circuits, the circuits are all designed to be able to output a high voltage pulse. The following section explains the construction, operation, and SCOS measurements associated with each high voltage circuit, with an emphasis placed on the versatility of the SCOS sensor in measuring high voltage systems.

6.1 Ignition Coil Circuit

In the last chapter, a modified ignition coil circuit is introduced as a periodic HV input to a capacitor charging/discharging circuit. Here, the output of the ignition coil circuit is measured using the SCOS sensor.

6.1.1 Measuring the Ignition Coil Circuit Output

Figure 6-1 shows the measurement setup for measuring the ignition coil using a SCOS and a parallel plate electrode. As before, the function generator supplies a 175 Hz square wave output and the parallel plates are spaced far enough apart to avoid arcing between the two plates.

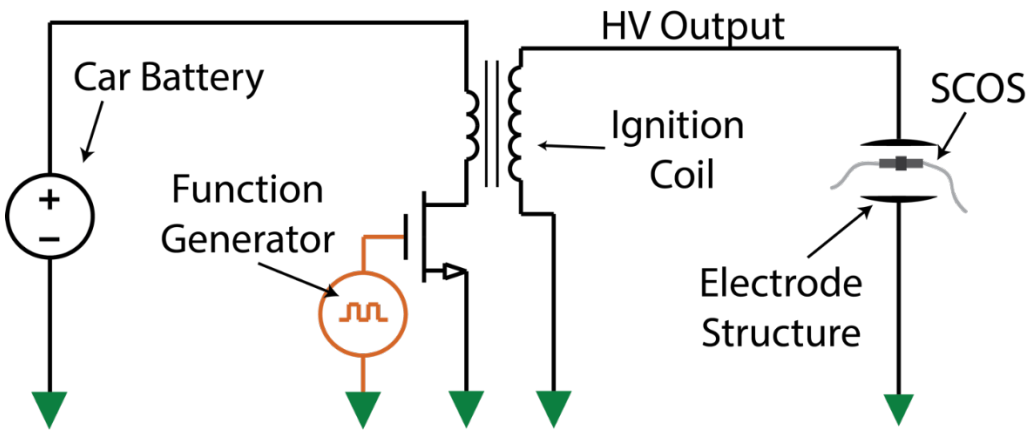

Figure 6-1. Measurement setup used to measure the output of the ignition coil circuit.

Figure 6-2 shows the output of the ignition coil circuit using the SCOS sensor. When the function generator supplies a rising edge to the gate of the MOSFET, the ignition coil experiences a surge of current from the battery (at t=0). The ignition coil acts more or less as an inductor, and the large spike in current creates a corresponding large voltage spike across the primary. Since the entire coil acts like a step-up transformer, the voltage on the primary induces higher voltage across the secondary, producing peak voltages as high as 41 kV on the output.

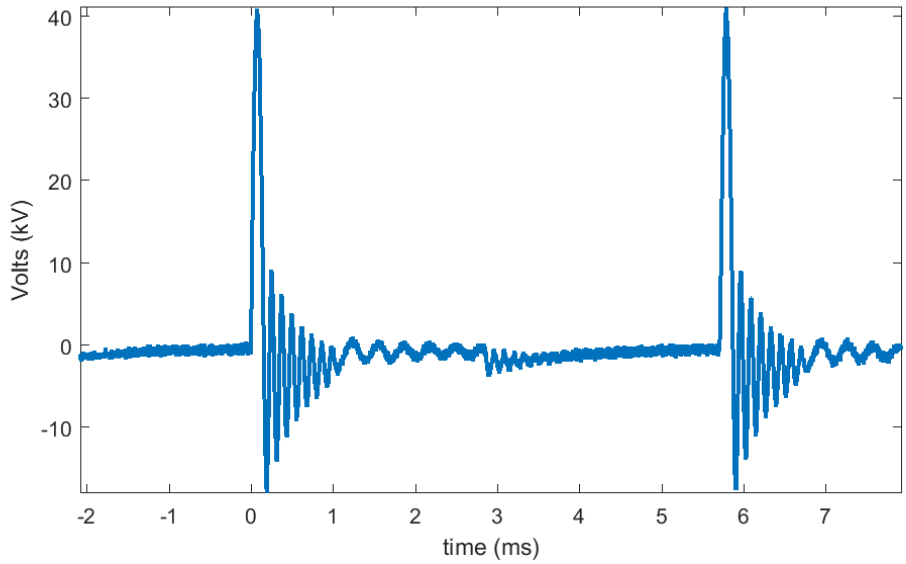

Figure 6-2. Single ignition coil output measured using SCOS.

6.1.2 Dual Ignition Coil Circuit

The SCOS is also used to measure the output of a 'dual ignition coil circuit'. The 'dual ignition coil circuit' operates in a similar fashion to the single ignition coil circuit shown in Figure 6-1 but has a higher voltage output. Figure 6-3 shows the dual ignition coil schematic, which consists of adding a second MOSFET-ignition coil system and placing the secondary coils in series, both MOSFETs can operate simultaneously. As the primary coils induce higher voltages on the secondary coils, the voltages on the secondary coils add constructively, creating significantly higher voltage on the output of the system.

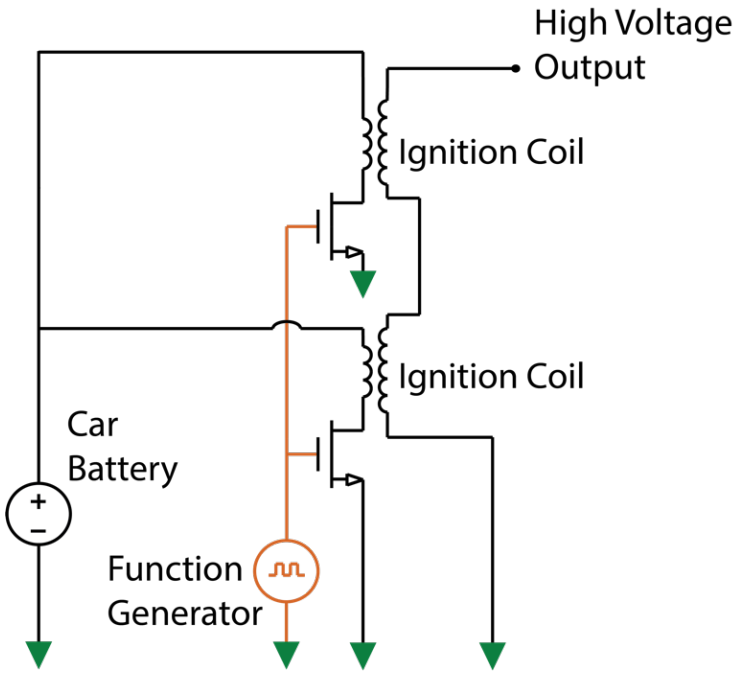

Figure 6-3. Dual ignition coil circuit schematic.

Figure 6-4 shows the output of the dual ignition coil circuit measured by the SCOS sensor. The output is much higher than that produced by a single ignition coil, outputting peak voltages of about 62 kV. The damping characteristics of the dual ignition coil circuit is slightly different from those produced by the single ignition coil circuit, and the SCOS is able to capture both clearly.

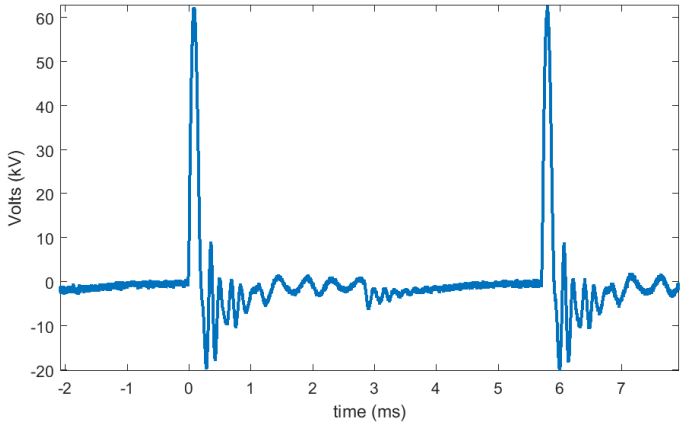

Figure 6-4. Output of dual ignition coil circuit measured by SCOS.

6.2 Marx Generator

6.2.1 Operation

In addition to the ignition coil circuit, SCOS can measure the high voltage associated with a Marx generator circuit. The Marx generator is a well-established, high voltage circuit and has been used in a variety of high voltage applications, such as X-ray machines, rail gun systems, etc. Construction of a Marx generator can incorporate a variety of components and component values. Although the traditional Marx generator design utilizes spark gaps, resistors, and capacitors, other configurations exist and range from inductors or liquid resistors instead of traditional resistors [47] to using BJTs or IGBTs instead of spark gaps [48,49,50,51,52]. Whatever the configuration, the basic operation of the Marx generator is the same. The Marx generator operates by charging a set of capacitors in parallel and then discharging those capacitors in series. Figure 6-5 shows a traditional schematic of a Marx generator. The high voltage DC source at the far left of the schematic supplies *k* volts to the system, which eventually charges each of the capacitors in the circuit to a voltage of *k* volts. R_c components represent 1 MΩ charging resistors, which allow the capacitors to charge to *k* volts but also provide enough

electrical resistance that they essentially appeared as an open circuit during the eventual discharge of the generator. 'SG' represents a spark gap, which consists of two wires separated by an arbitrary gap distance. This gap distance is large enough to prevent premature arcing but small enough to reliably arc during discharge.

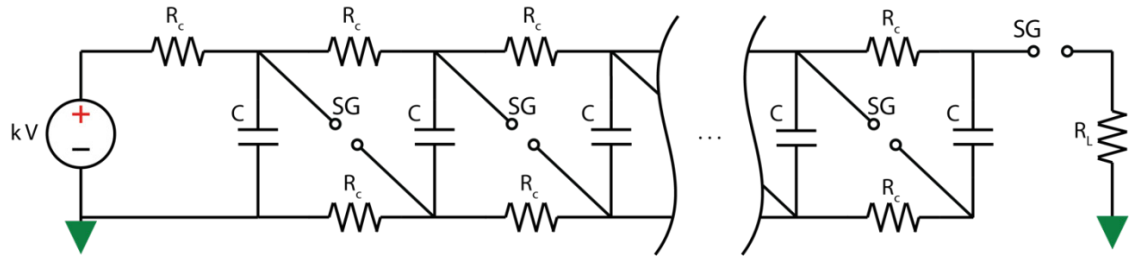

Figure 6-5. Schematic of a Marx generator. Each capacitor represents a stage in the circuit.

When the Marx generator is charging, the spark gaps are considered open circuits and the capacitors collect charge. Figure 6-6 shows the effective circuit during the charging phase. During this phase, each of the capacitors are charged to a voltage of *k* volts.

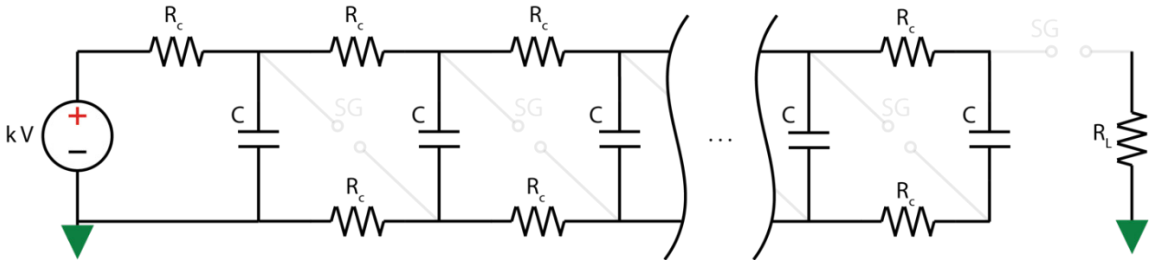

Figure 6-6. Charging of a Marx generator circuit. At this point, each of the capacitors are charged to k volts.

Once each capacitor has been charged to *k* volts, the Marx generator is discharged. Figure 6-7 shows the effective circuit during the discharge phase. This occurs when the 1st spark gap (spark gap between point *a* and *b*) is shorted, which raises the voltage potential at *b* from ground to *k* volts (the voltage of point *a*). This causes the voltage at point *c* to rise from *k* volts to 2*k* volts. Since the potential at point *d* is zero, the voltage potential between point *c* and *d* is 2*k* volts, and second spark gap arcs, pushing the voltage at point *d* from zero to 2*k volts. As this

process propagates through the rest of the circuit, the voltages of the capacitor essentially sum together. The load (R_L) therefore sees a voltage of $n*k$ volts, for an n-stage Marx generator with an input DC voltage of k volts.

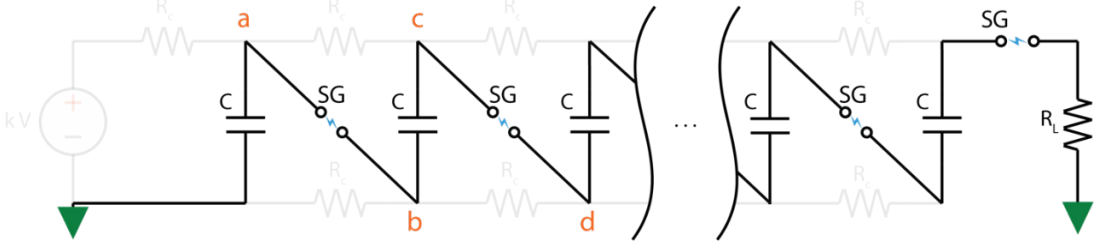

Figure 6-7. Discharging of the Marx circuit. As the voltage arcs across the first spark gap, the potential across the second spark gap jumps to 2k volts, which results in air breakdown across the second spark gap. Likewise, as the second stage arcs, the potential across the third capacitor exceeds breakdown. This continues until all the voltage potential is summed and discharged through the load.

Figure 6-8 shows the arcing of a simple 10-stage Marx generator. The red blocks are high voltage capacitors and the brass balls are the spark gaps. A tank of transformer oil houses the generator which reduces corona, and an aluminum disk acts as a triggering electrode which discharges the Marx generator. Although each stage is only charged to 10 kV, the voltages of each stage sum together and produce a much larger output. The last (right-most) arc between the last brass ball and the red alligator clip is the output of the circuit.

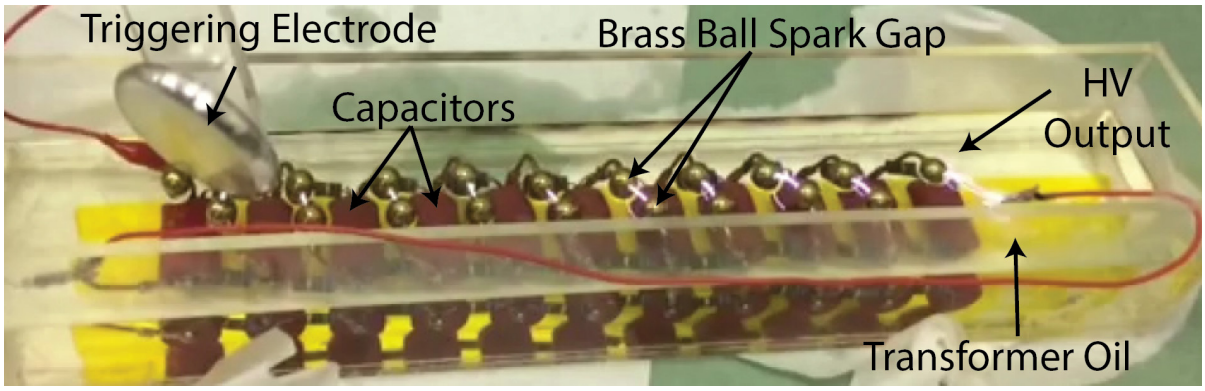

Figure 6-8. Arcing of a 10-stage Marx generator. After the voltage is charged up on each of the capacitors, the circuit is triggered via an aluminum triggering electrode. The energy is discharged in via the brass spark gaps, resulting in a high voltage discharge at the HV output of the Marx generator. Upon discharge, the voltages of each stage sum together and arc at the output (largest arc on the right).

6.2.2 Measuring the Output Using SOCS

An electrode structure with a SCOS inside (not pictured) connects to the output of the 10-stage Marx generator to measure the generator's final voltage output. Figure 6-9 shows these measurements. The sharp rise time is associated with the quick arcing of each of the spark gaps. As the spark gaps arc together, the capacitors discharge in series with each other, and their voltages sum together to a total of 52 kV. The fall time appears to be a combination of two or more RC time constants. Theoretically, a 10-stage Marx generator with an input of 10 kV should output a 100 kV arc. However, the measurements show a generator output that is much lower than expected.

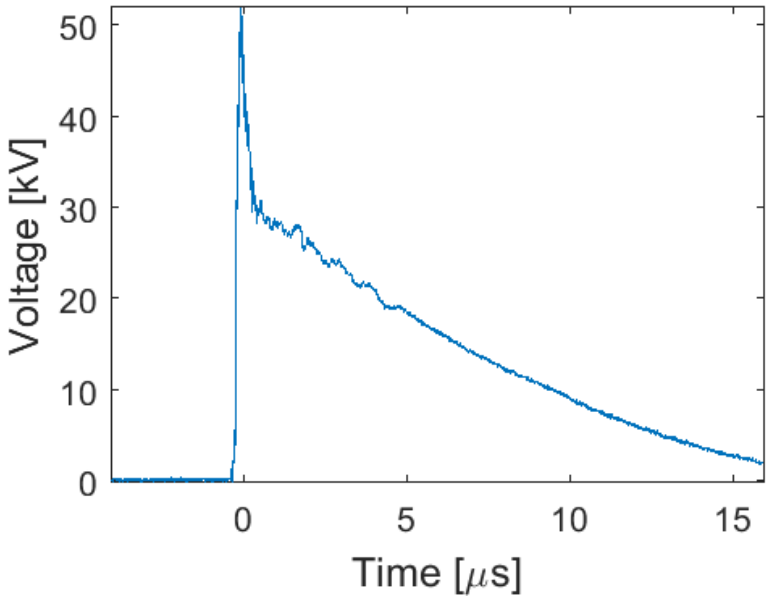

Figure 6-9. Output measurement of the last stage of the Marx generator.

The SCOS also assists in troubleshooting the performance of the Marx generator. Since the measurements in Figure 6-9 show a large discrepancy between real and expected voltage outputs (52 kV and 100 kV, respectively), a SCOS measures the voltage on each of the stages of the Marx generator. This is done in the hopes of discovering which stage or stages are not

performing properly. An electrode structure with a SCOS inside connects to each stage shown in Figure 6-5, and the SCOS records the voltage values across each spark gap. Figure 6-10 shows the peak values of these measurements, which are an average of 5-6 separate measurements done at each stage. An error bar is also included at the top of each bar which shows the range of the measurements taken. Although the voltages on the first few stages appear to perform as expected with the voltage increases by about 10 kV for each successive stage, the voltage increase attenuates during later stages. This might be attributed to a number of circumstances including corona losses within the system, the DC supply not being able to provide enough current to fully charge later capacitors, spark gaps not triggering properly, etc.

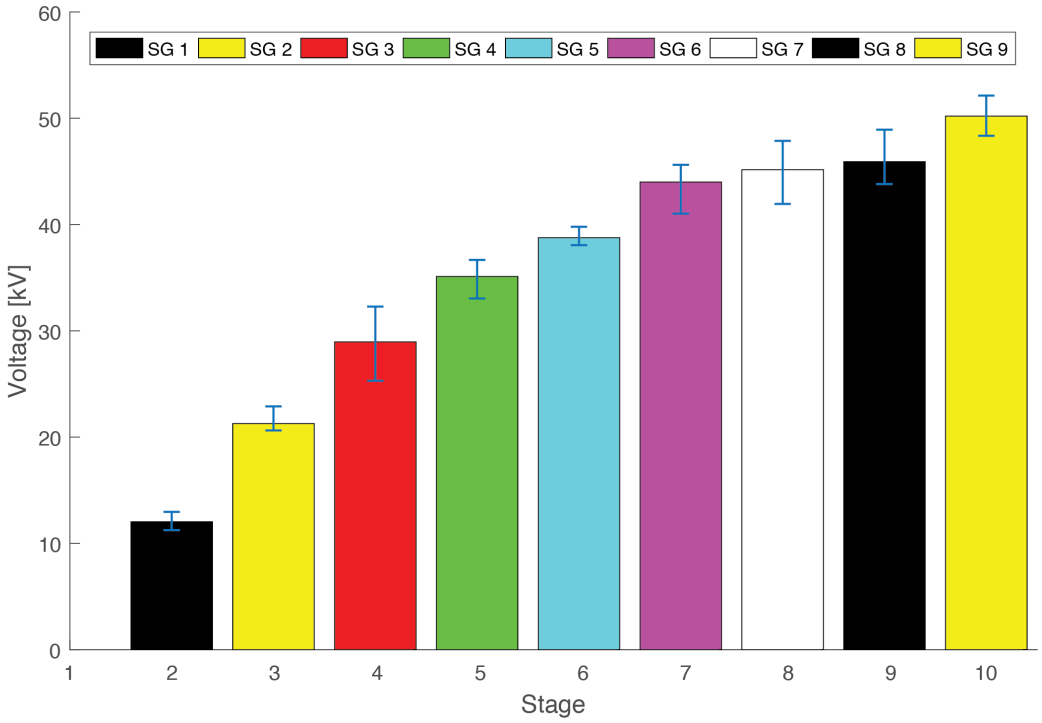

Figure 6-10. Voltage measurements taken on each stage of the Marx Generator. SCOS are able to be used as a tool to troubleshoot high voltage systems such as this Marx generator.

The Marx generator operates through a series of high voltage arcing. These arcs often introduce unwanted EMI to measurement. SCOS, however, can characterize high voltage signals without being largely affected by these types of interferences.

6.2.3 Exploring Possibilities for Output Discrepancy Using SCOS

There might be several reasons the Marx generator shown in Figure 6-8 outputs a much lower voltage than expected. These may include too much inductance in the system, corona losses preventing each stage from completely charging to 10 kV, or the system simply not being able to store enough energy. One of the most likely reasons we expect the Marx is not performing as well as expected is due to possible triggering timing errors within the stages. To test this theory, a SCOS measures the output (after the 10^{th} stage) of the Marx generator, while a second SCOS simultaneously measures the output of the 1^{st} stage. As the Marx generator is discharged, the time delay between the 1^{st} stage and the final output is recorded. Measurements are repeated (about 5-7 times) for each stage (1^{st} through 9^{th}) so that the time delay between each stage and the output can be determined. Figure 6-11 shows the results of these tests. These results suggest that each stage does not trigger simultaneously. Rather the discharging tends to propagate from the first stages until the output. Moreover, the time delay varies significantly within the first couple stages, which might indicate inconsistent triggering since the operator triggers the first stage manually using the triggering electrode shown in Figure 6-8. Also, the 7^{th} stage (white) consistently discharges earlier than stages 5 and 6 (teal and pink respectively) rather than between the 6^{th} and 8^{th} stage (pink and black respectively). These variances in discharge times may play a role in the Marx generator outputting a lower voltage than expected.

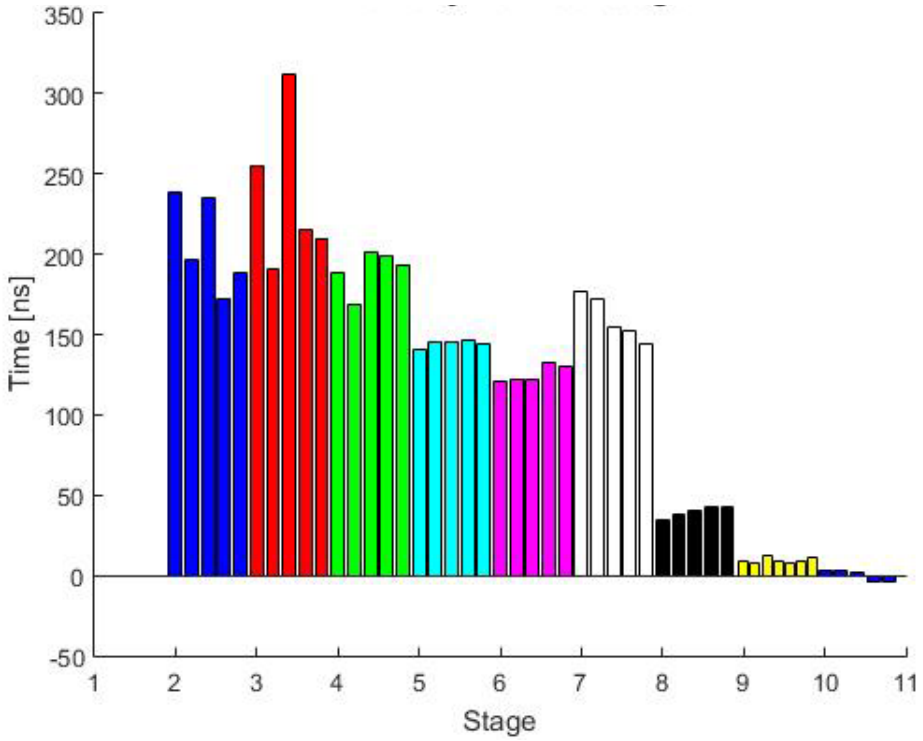

Figure 6-11. Time delay of each stage before the output of the system (10th stage) was observed. Measurements of each stage were taken anywhere from 5-7 times each and are shown side by side for comparison.

The SCOS is capable of being used as a troubleshooting tool during the high arc dynamics of a Marx generator and can offer valuable insight into the operation of HV arc systems.

6.3 200 kV HV Generator

Due to issues of being unable to produce voltages higher than 50-60 kV reliably using the ignition coil circuit in Section 6.1 and the Marx generator in Section 6.2, a voltage arc generator capable of generating 200 kV arcs was built. This system utilizes a variable autotransformer (Variac), two 50 kV DC supplies, two 35 nF HV capacitors, a charging resistor, and a series of switching mechanisms.

6.3.1 Schematic and Operation

Figure 6-12 shows the schematic of this generator. The negative terminal of one of the 50 kV supplies (Vdc2) and the positive terminal of the other 50 kV supply (Vdc2) connect to ground. Since the Variac supplies power to the two 50 kV supplies, adjusting the level of the Variac adjusts the output of each of the 50 kV supplies. The HV output can therefore be scaled to output a desired voltage between 0 and 200 kV. The switches allow the circuit to transition between the charging phase (position 1) and the discharging phase (position 2).

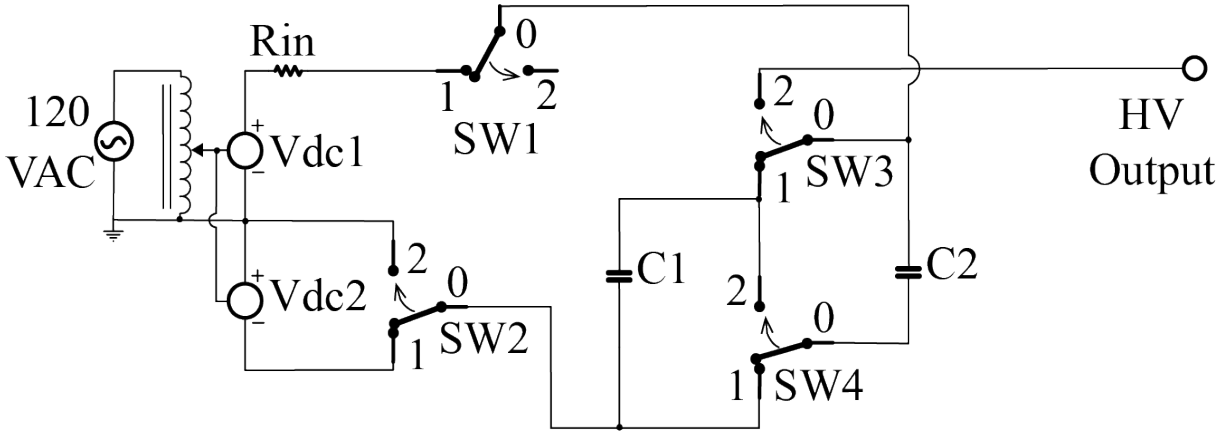

Figure 6-12. Schematic for 200 kV arc generator.

Figure 6-13 shows the effective schematic of the charging phase when the switches are in position 1. In this phase, the HV capacitors (C1 and C2) have +50 kV (from Vdc1) applied to one of their terminals and -50 kV (from Vdc2) applied to the other terminal, creating a potential difference of 100 kV across each capacitor. Once the capacitors are fully charged via the charging resistor (Rin), the switches can switch to position 2 for generator discharge.

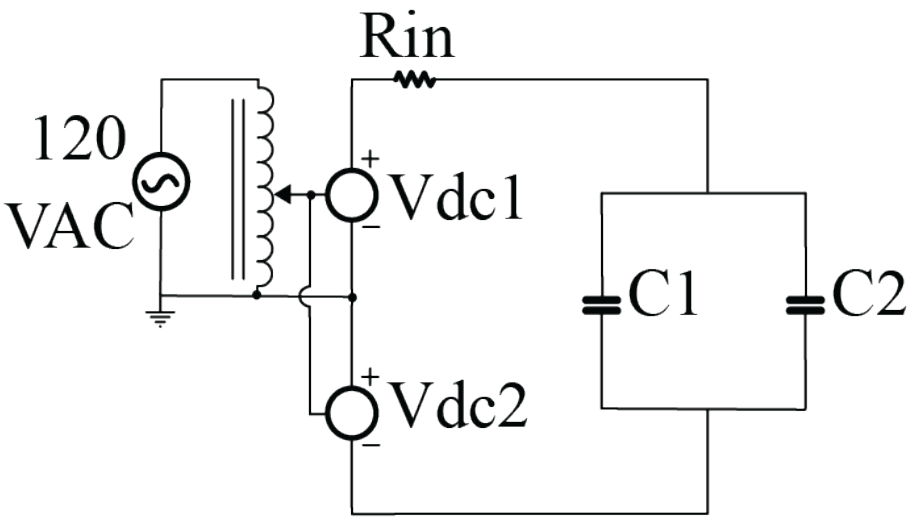

Figure 6-13. Schematic of Figure 6-12 when the switches are in position 1 (charge phase).

Figure 6-14 shows the discharge phase of the circuit when the switches are in position 2. During this phase, the capacitors disconnect from Vdc1 and Vdc2 and are in series with each other. The negative terminal of C1 then connects to ground and the positive terminal of C2 becomes the output of the circuit. If, for example, the charge placed on each of the capacitors is 100 kV (-50 kV to +50 kV) between the terminals during the charging phase, the voltage on the capacitors sums together during phase 2 and the circuit outputs +200 kV.

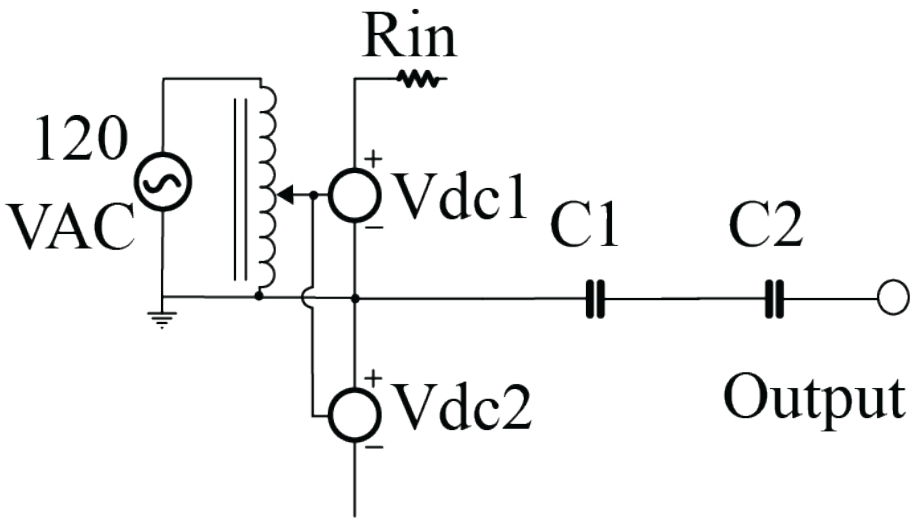

Figure 6-14. Schematic of Figure 6-12 when the switches are in position 2 (discharge phase).

6.3.2 Custom Switches

In order for the 200 kV circuit to operate properly, four separate switches needed to be implemented. By making custom switches, the switching process was simplified. Each of these switches contain two of the switches shown in Figure 6-12. Combining these switches allows the operator to switch both SW1 and SW2 using a single custom switching mechanism, as well as switch both SW3 and SW4 using another custom switching mechanism. Thus, the 4-switch switching process outlined in Figure 6-12 can be simplified to the operation of just two switching mechanisms. Figure 6-15 shows one of these custom switching mechanisms. This mechanism has an acrylic frame with a nylon rod with brass connections placed on either end of the rod. This nylon rod can snap into 'up' or 'down' positions by clipping into two plastic clips on the top and the bottom and is guided via a groove cut into the back of the frame. The brass connections on the ends of the rod connect to the HV capacitors via copper wires coated with a white, transformer oil-resistant jacket. When the rod is in the 'down' position, the brass cups make contact with smooth, brass electrodes, and the capacitors collect charge. When the rod is in the 'up' position, the system is in the discharge phase, and the brass cups make a more secure contact with the brass balls toward the top of the frame. The entire switching mechanism operates with a single polyethylene rod (not shown) that hooks onto the nylon rod. By a single motion of the operator's arm, two contact switches can be simultaneously controlled, making the procedure of the generator simpler and faster for the operator.

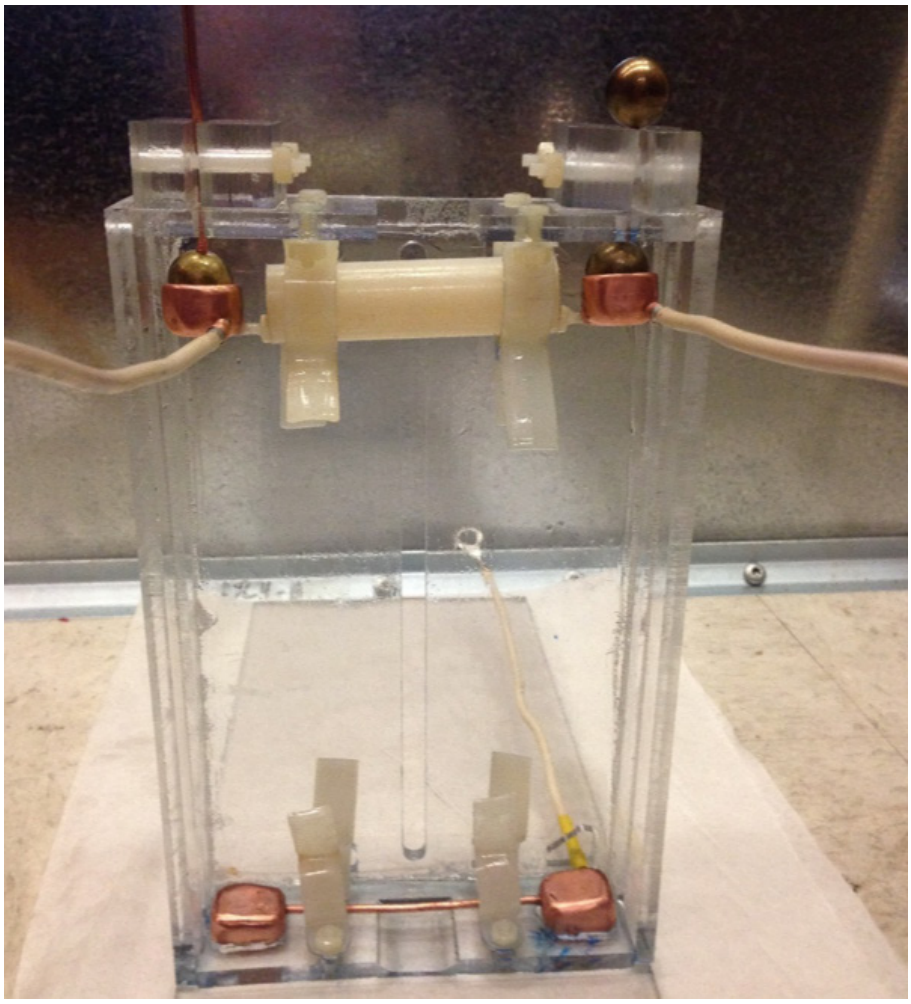

Figure 6-15. One of the custom switching mechanisms used in the 200 kV generator.

During the charging phase of the generator, the bottoms of the brass cups create a connection with the brass electrodes on the bottom of the acrylic structure. Figure 6-16 shows this contact. Since the current used to charge the system is relatively small ($\leq$ 5 mA), this simple connection provides sufficient electrical contact. The plastic clips visible in Figure 6-15 hold this electrical connection in place. To prevent corona losses and unwanted arcing, the copper cup, bottom copper electrode, and the wire connection point have been rounded and sanded.

Figure 6-16. Surface contact for ‘down’ position for the switch shown in Figure 6-15. The flat base of the copper cup creates adequate contact with the bottom brass electrodes during the charging phase.

During the discharge phase, the current through the system is much larger than during the charging phase. To ensure optimal electrical contact during this phase, the cups allow for a large surface area contact with the top brass sphere electrodes. Figure 6-17 shows this cup and ball contact. The cup was filled with solder and molded to the shape of the brass sphere.

Figure 6-17. Surface contact for ‘up’ position for the switch shown in Figure 6-15. The molded solder-filled copper “cup” ensured optimum contact with the brass ball during the discharge phase.

6.3.3 DC Operation of Assembled Generator

To reduce corona and unwanted arcing within the system, a tank of transformer oil houses the 200 kV generator. Figure 6-18 shows the assembled 200 kV generator placed in the oil. ‘Switch 1/2' represents SW1 and SW2 from Figure 6-12, and ‘Switch 3/4' represents SW3 and SW4 from the same figure. The ‘Triggering Switch’ is an additional switch that connects to the ‘HV Output’ in Figure 6-12 which allows separate triggering of the HV output from the operator.

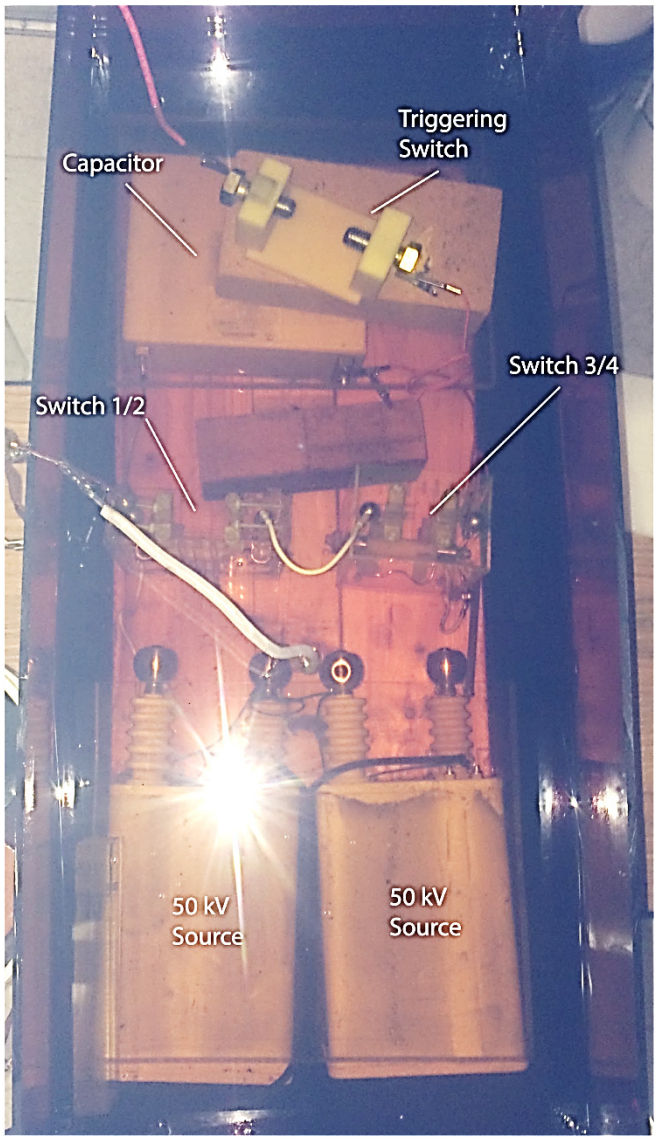

Figure 6-18. Assembled 200 kV generator placed in a container of transformer oil. Individual components are labeled.

To verify that the system works properly, a resistive voltage divider measurement tests the DC output of the final system. To measure this output, the voltage divider records the output of the 200 kV generator for various input RMS settings from the Variac. Figure 6-19 shows the output of the generator as a function of input RMS from the Variac. Compared to the expected output voltages, the actual voltages as measured by the voltage divider verify that the system works as designed, only varying slightly from the expected results.

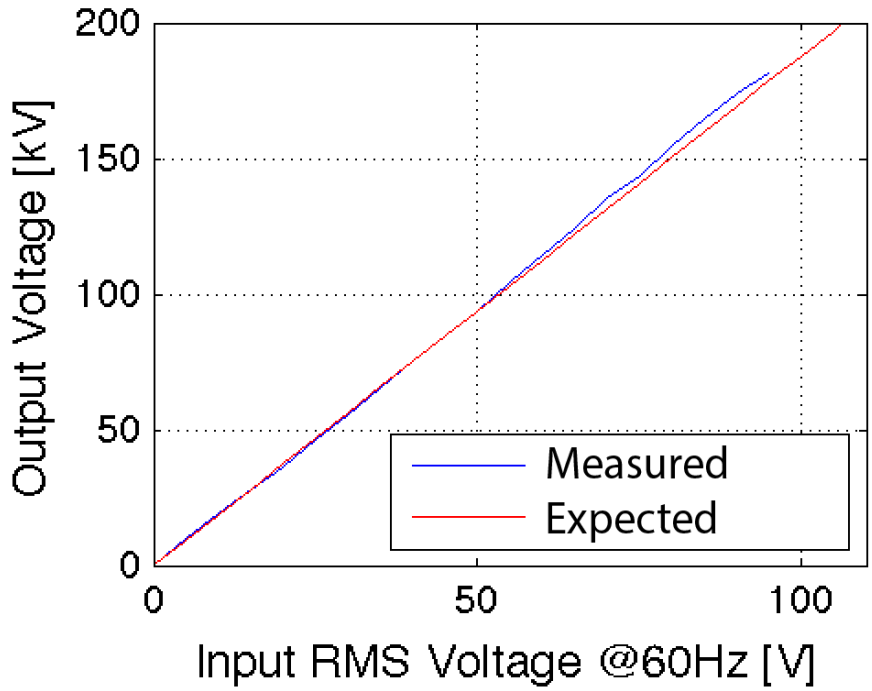

Figure 6-19. Measured and expected output voltages of the 200 kV generator as a function of input RMS voltage as supplied by the Variac.

6.3.4 Testing Speed of SCOS

The high voltage generator discharge helps demonstrate the speed of the SCOS. This is done by measuring the output voltage of the high voltage generator as the generator charges to 42 kV and then discharges through a resistive load. Since the output of the generator is 17.5 nF (two 35 nF capacitors in series). Figure 6-20 shows a simplified version of this discharging circuit, which shows the effective discharging circuit with the SCOS in place. After we calibrate the system as previously described, the capacitors, in series, collectively charge to 42 kV and have an effective capacitance of 17.5 nF. At t=0, the effective 17.5 nF capacitor bank has 42 kV and disconnects from the high voltage DC supplies. At this point, switch 1 opens and no current flows through the circuit. Shortly after, at t=1, switch 2 closes, which allows the SCOS within the electrode structure to capture the voltage on the capacitor as current flows through the 100 kΩ resistor.

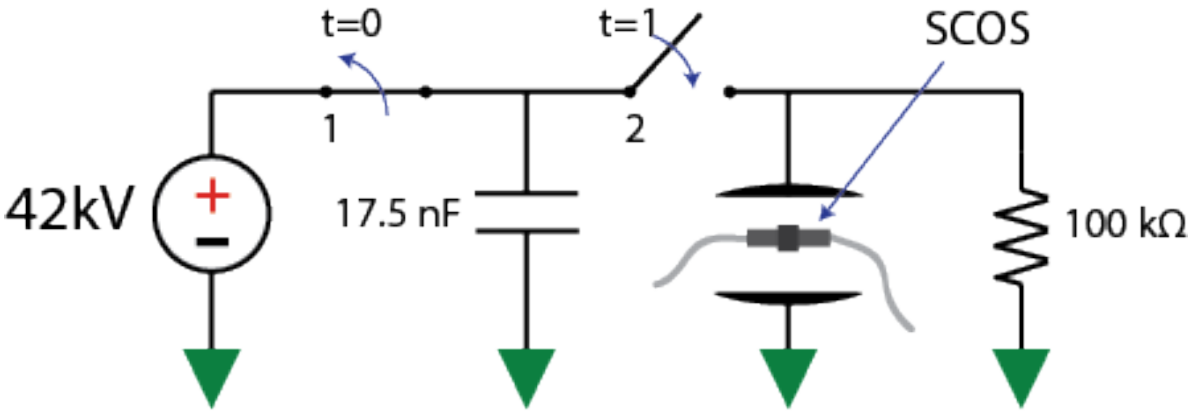

Figure 6-20. Capacitor charging and discharging circuit. At t=0 the capacitor has a voltage of 42kV, and switch 1 opens, causing no current to flow within the circuit. At t=1 switch 2 closes, causing current to flow through the RC circuit while the SCOS measures the voltage on the capacitor during the discharge.

Figure 6-21 and Figure 6-22 show the voltage captured by the SCOS after applying the calibration factor. This is the RC discharge of the circuit. As expected, when switch 2 closes, the voltage as seen by the SCOS sensor rises sharply. The theoretical RC time constant of the circuit is the capacitance seen by the electrode structure (approximately 17.5 nF) multiplied by the resistance seen by the electrode structure (approximately 100 kΩ). This calculation results in a theoretical value of 1.75 ms, which matches the observed time constant shown in Figure 6-21. Figure 6-22 shows the initial rise time of the SCOS for the results shown above in Figure 6-21. Through this setup, we are able to obtain rise times as low as 6.6 ns. It should be noted that the ringing in Figure 6-22 is most likely caused by parasitic inductance in the system and/ or transmission line effects due to impedance mismatches. Measures are not taken to improve the ringing simply because the purpose of the measurement is to demonstrate a relatively sharp response of the SCOS.

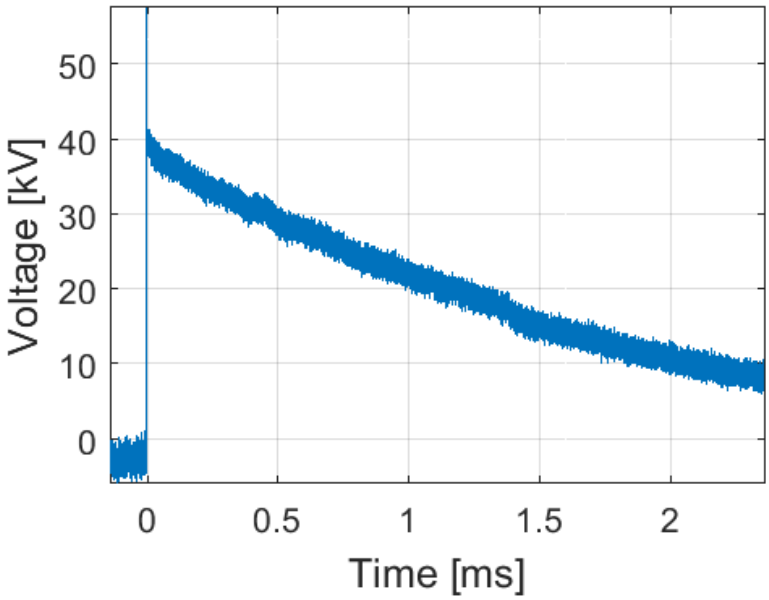

Figure 6-21. SCOS measurement of the capacitor discharge circuit.

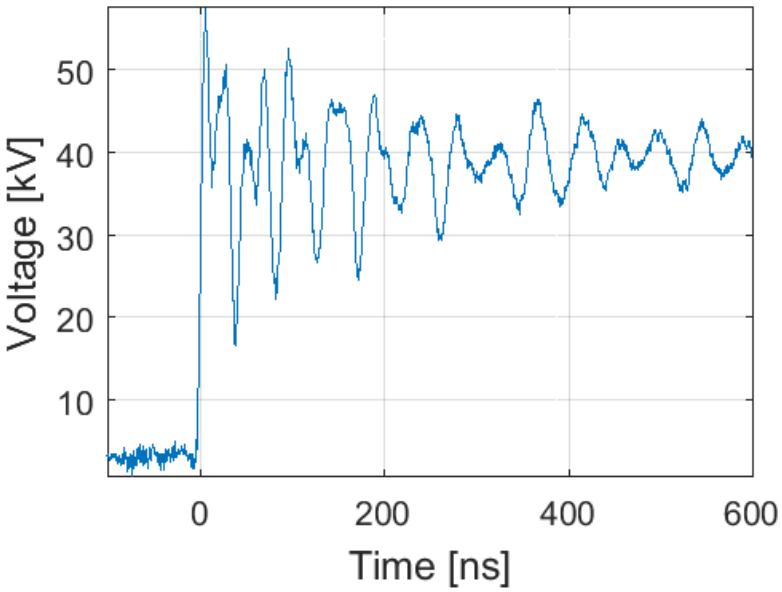

Figure 6-22. Zoomed in view of the measurement in Figure 6-21 to show a rise time of 6.6ns.

SCOS are also able to record a dynamic range of high voltages. Figure 6-23 shows SCOS measurements of the circuit shown in Figure 6-20 with the input voltage varying from 22.2 kV to 111 kV. The SCOS is able to accurately capture the discharge spectrum for voltages as high as 111 kV.

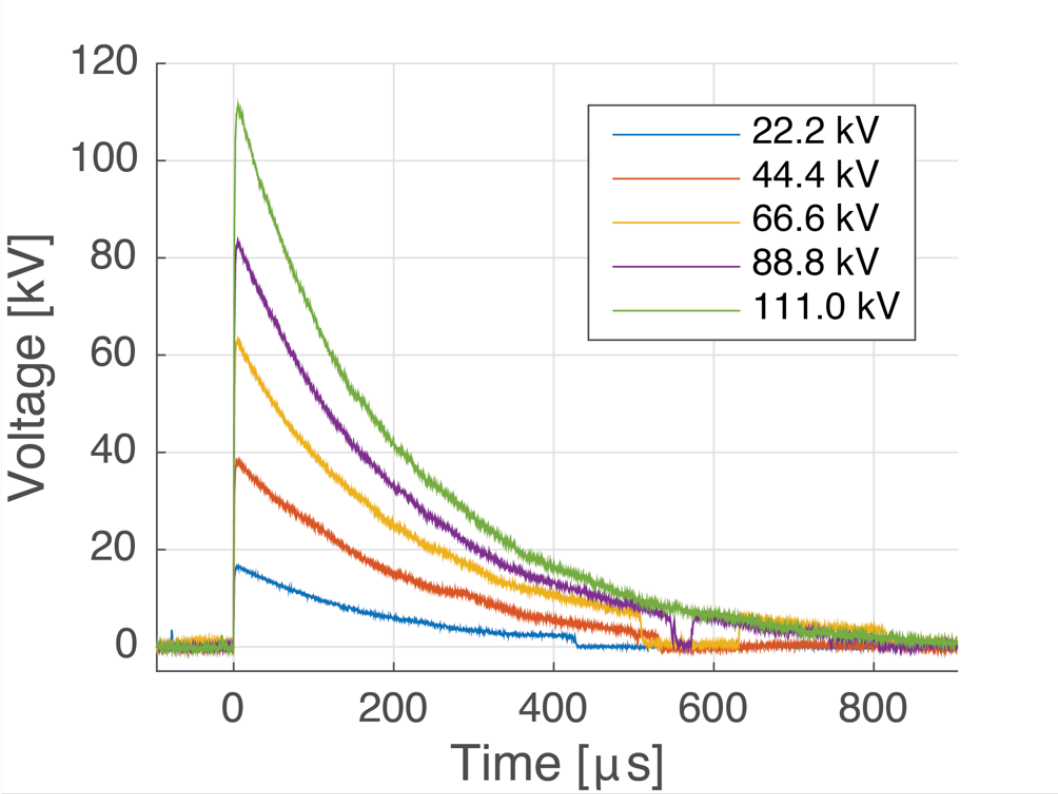

Figure 6-23. Capacitor discharges for various voltages using the circuit shown in Figure 6-20 and varying the input voltage from 22 kV to 111 kV.

7 CONCLUSION

The SCOS sensor offers an alternative way of measuring high voltage signals. Using a parallel plate structure and a known voltage source, we obtain a calibration factor, which can be used to characterize subsequent voltage measurements. SCOS offer an alternative way of measuring voltage signals optically. This is particularly useful when measuring higher frequency signals or signals that produce EMI, such as the case when a high voltage arc is produced.

SCOS sensors were used to measure voltage rise times of 6.6 ns and voltages of 111 kV as well as characterize other high voltage sources such as the modified ignition coil circuit, a Marx generator, and a high voltage capacitor discharge circuit. Since lithium niobate materials have a much higher corner frequency (~10GHz) [28], using faster supporting electronics could theoretically increase speed performance.

8 OTHER WORKS: FBG INTERROGATION ON HOPKINSON BAR

This section presents the method by which the strain along a Hopkinson bar specimen is optimized and reconstructed. Typically strain along a specimen within a Hopkinson bar is measured using strain gauges. Such measurements do not require a direct line of sight to the tapered specimen. However, these devices only provide an average of the strain along the specimen rather than an entire strain profile [11].

An alternative method involves using Digital Image Correlation (DIC) to visually capture the dynamic deformation of materials. Such methods can determine the entire spectrum of the specimen, but also require a direct line of sight.

An alternative method to using strain gauges or a DIC analysis is to use optical based strain sensors called fiber Bragg gratings (FBGs). By placing an FBG on the tapered section of the Hopkinson bar, the FBG can dynamically measure the strain profile along the specimen without the need for a direct line of sight.

8.1 Introduction to FBGs

Fiber Bragg gratings (FBGs) are a particularly useful tool in the realm of optical sensing. These sensors are fiber optic-based strain sensors that detect strain and respond by reflecting an optical spectrum.

The way FBGs work is fairly straight forward. These sensors contain a small (4-10mm) sensing region along the length of the optical fiber known as the "grating". A swept laser source shines down the fiber, and the grating reflects a Gaussian-like optical spectrum back toward the laser. Figure 8-1 shows an example of this spectrum, which has no strain applied across the grating.

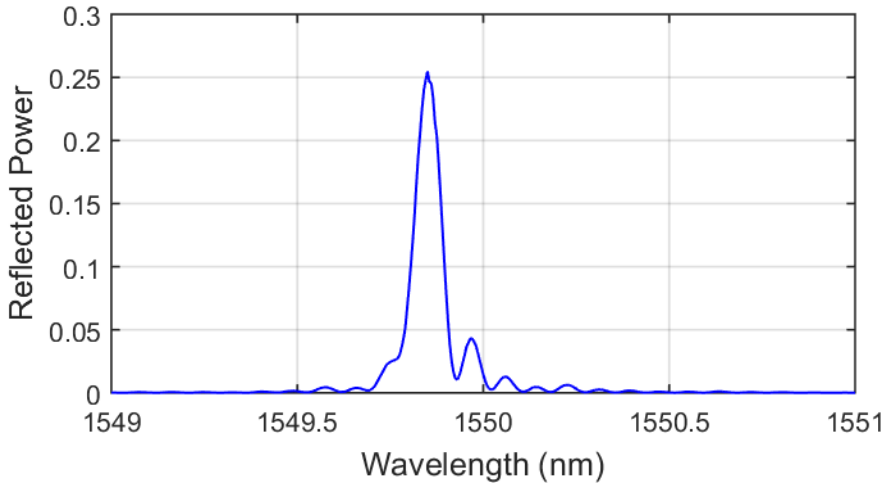

Figure 8-1. Example of a typical FBG reflection spectrum.

When the grating is exposed to strain (whether linear or nonlinear), the reflected spectrum distorts in response. Figure 8-2, Figure 8-3, Figure 8-4, and Figure 8-5 illustrate the resulting distortions and shifts in an FBG spectrum due to applied strain.

Since the strain along the grating is almost never known, the only key to find it lies buried within the FBG's reflection spectrum. The strain on the FBG could be constant (such as that shown in Figure 8-2 or it could be nonlinear, causing peak broadening, peak splitting, and virtually every kind of spectrum distortions (see Figure 8-2, Figure 8-3, Figure 8-4, and Figure 8-5). Solving for these various types of strain profiles involves being able to accurately model the strain along the length of the grating.

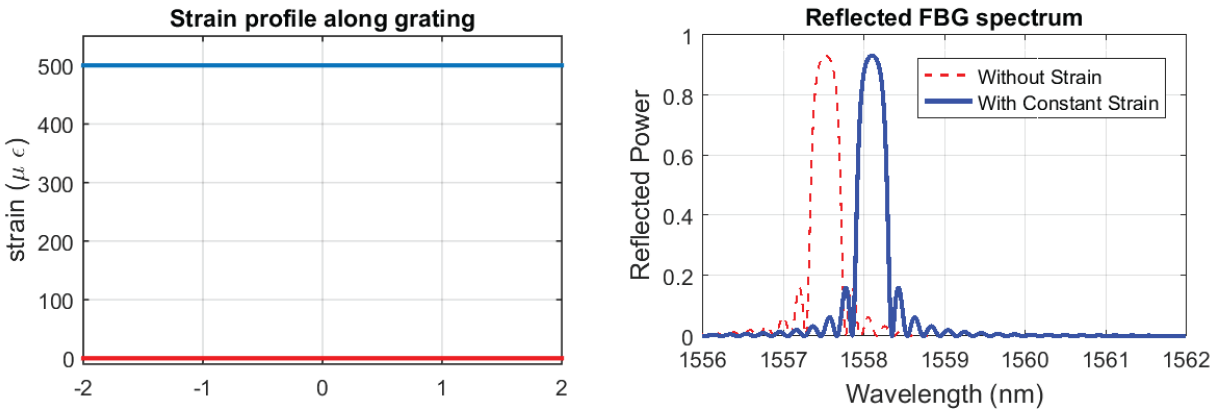

Figure 8-2. Constant strain profile along grating (left) and the resulting FBG spectrum (right).

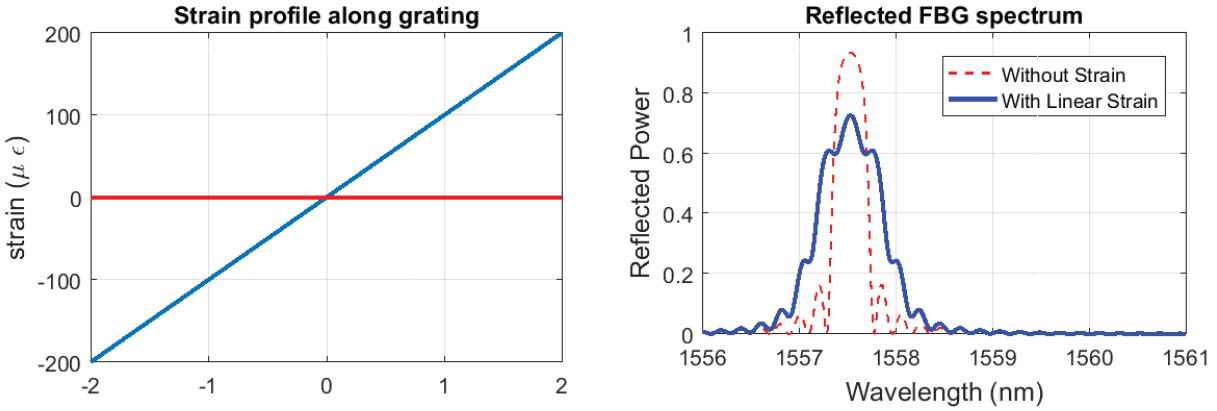

Figure 8-3. Linear strain profile along grating (left) and the resulting FBG spectrum (right).

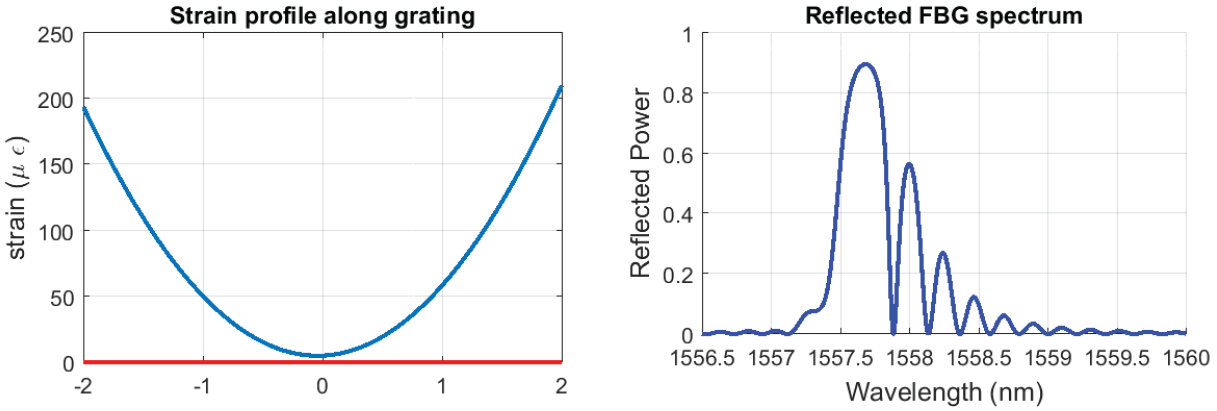

Figure 8-4. Quadratic strain profile along grating (left) and the resulting FBG spectrum (right).

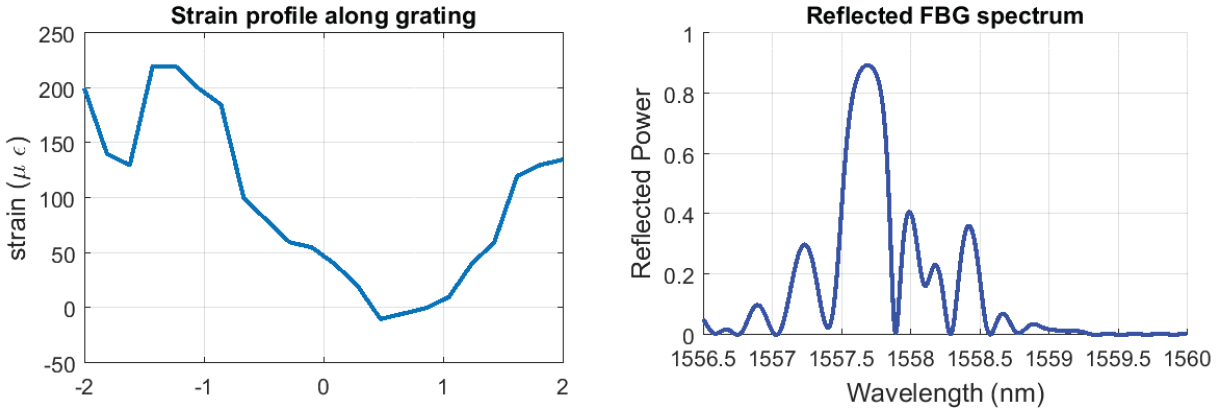

Figure 8-5. Random strain profile along grating (left) and the resulting FBG spectrum (right).

For relatively simple FBG measurements with only constant strain, simple peak detection algorithms will suffice to track movement (and therefore strain) on the FBG. Although simple peak tracking approaches are useful and convenient, they fail to report the full and detailed strain along the FBG's grating when the FBG is under more complex strain.

Applying various complex strain configuration to the FBG will result in radically different reflection spectrums that cannot be characterized by simple peak tracking methods. We must do rely more heavily on theoretical models to extract more complex strain profiles.

Modeling the spectrum of an FBG is not as trivial as you might initially expect. Multiple methods have been used to model such a system including the Runge-Kutta method and the transfer matrix (T-matrix) method.

The Runge-Kutta method is a more technical method to model FBGs, and it delves into the nuances of coupled-mode and optical waveguide theory [54]. The T-matrix model is a tested form of modeling the theoretical reflection response of an FBG when exposed to strain. This technique has been developed over the years and is particularly known for its ability to be computed relatively quickly compared to other methods [55,56]. Though still complex in nature,

the T-matrix model attempts to make general simplifications, providing computational speed in exchange for potential over-generalizations [57].

8.1.1 The T-matrix Model

The T-matrix is used to compute the reflection spectrum given a specific FBG and strain profile. However, the inverse problem involving taking the reflection spectrum and determining the strain profile is more difficult. The strain profile is optimized along the FBG grating by adjusting the strain profile until the calculated reflection spectrum matches the measured spectrum. The strain along the grating can be linear or nonlinear, and optimization is used to solve for the strain profile along the grating of an FBG. While past efforts have developed theoretical models to suggest possible FBG spectrums for a given strain profile, this paper explains how an optimizer was used to work backwards from the typical approach, extracting an unknown strain profile from a measure FBG spectrum. This optimization process is used to identify the strain along an FBG as it dynamically records the strain on a Hopkinson bar during impact [11].

In the T-matrix model, the overall shape of the FBG is a result of a number of system parameters. Although the details will not be explained here, the overall idea is that the FBG grating is represented by a discrete number of sections. For a given wavelength, each section is represented by a 2 × 2 matrix,

$$F_i = \begin{bmatrix} A_{11} & A_{12} \\ A_{21} & A_{22} \end{bmatrix}, \tag{8-1}$$

where A_{11}, A_{12}, A_{21}, and A_{22} are functions of wavelength, physical parameters of the FBG, as well as strain applied along the grating. Each section contributes to the magnitude of the reflection seen at each wavelength. For a given wavelength, these sections are then combined such that

$$F_{final} = \begin{bmatrix} R_{11} & R_{12} \\ R_{21} & R_{22} \end{bmatrix} = \prod_{i=1}^{n} F_i \ , \tag{8-2}$$

where F_i is the matrix of each grating section as described in Eq. (8-1). The total resulting reflection at a given wavelength is then defined as $R(\lambda) = \left|\frac{R_{21}}{R_{11}}\right|^2$.

Essentially, if we were to represent the FBG grating by 100 discrete sections and have 1000 wavelengths that we wish to sample, the T-matrix model would first create a total of 100,000 2 × 2 matrices, 100 matrices (like those in Eq. (8-1), for each wavelength we wish to evaluate. Each of the 100 matrices for each wavelength is multiplied by one another as outlined in Eq. (8-2) to form a single 2 × 2 matrix from which the reflected power at that particular wavelength can be calculated. This process is repeated to find the reflection at the other wavelengths. Computing Eq. (8-2) for each wavelength creates our simulated spectrum similar to that shown in Figure 8-1. The merit function used for our optimization is then simply the variance between the simulated spectrum and the measured spectrum.

8.2 Hopkinson Bar and Test Setup

The split-Hopkinson bar was originally developed by Kolsky and is a tool to test high strain rate in materials such as metal, concrete, and ceramics [58,59,60]. Figure 8-6 shows the basic operation and measurements setup of a split-Hopkinson bar. The bar operates by a weight (such as an anvil) striking the incident bar, which causes stress waves to propagate through the bar. The operator places a specimen of the material to be tested (in this case, a tapered aluminum specimen) in between the incident bar and the transmitted bar. As the strain caused by the anvil propagates along the bar the specimen undergoes strain.

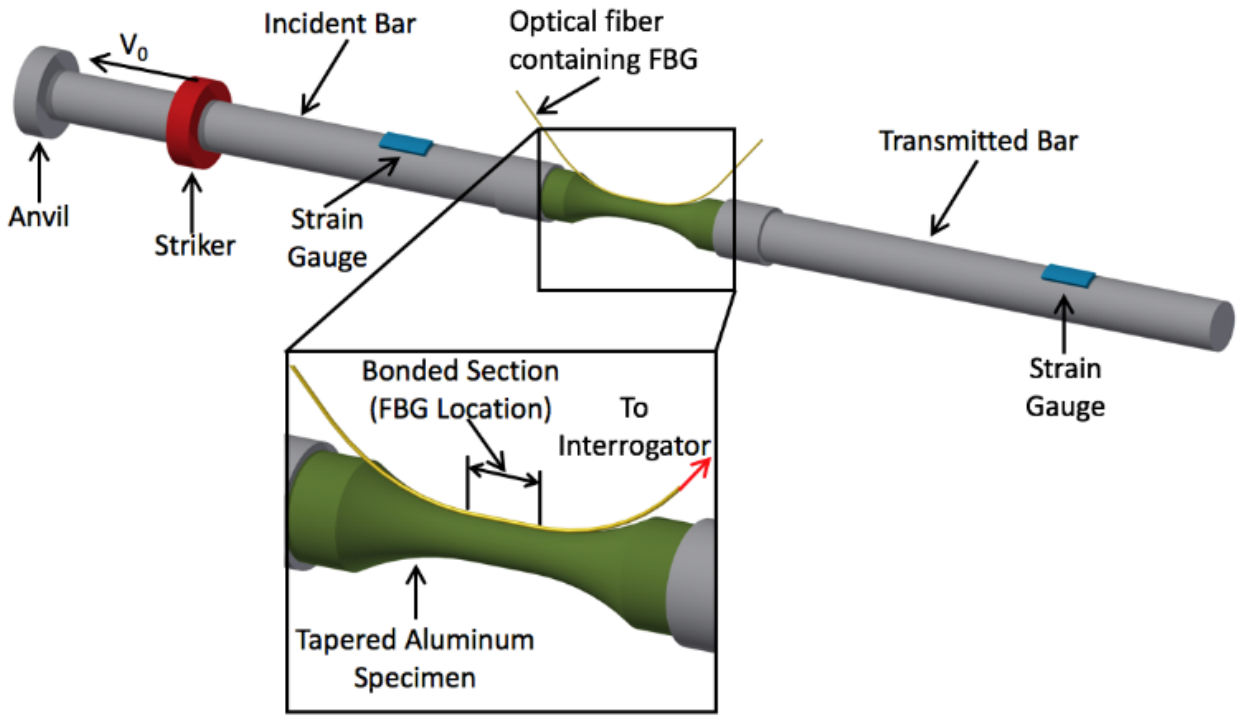

Figure 8-6. Split Hopkinson tensile bar with a tapered section (green). As stress is applied to the bar, the stress propagates through the tapered section and produces strain. The strain within the tapered section is measured using an FBG which is bonded to the section. The strain is recorded via strain gauges (blue) as well as visually using DIC software (not pictured) [11].

The system is interrogated using an Insight swept source laser that samples the FBG spectrum at a frequency of 100 kHz (every 10 μs) with a wavelength resolution of about 25 pm. The FBG spectrums over time can then be individually analyzed and the strain profile along the grating can be found using the optimization methods discussed previously. Figure 8-7 shows some examples of successive spectrums as well as their optimized strain profiles. The optimized strain profiles (left, red dashed) correlate well with the actual profile (left, blue).

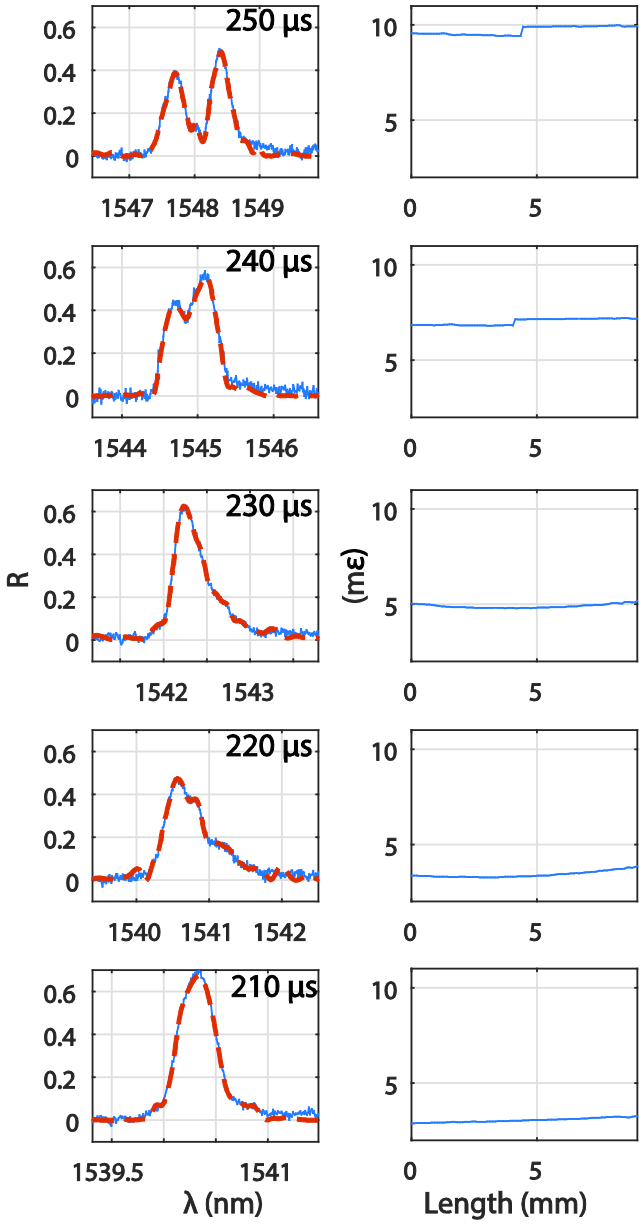

Figure 8-7. Actual FBG spectrums (left, blue) with their corresponding spectrums found through optimization (left, red dashed) and their optimized strain profiles (right) [11].

The optimized strain profiles seem to correlate well with the strain profiles obtained using a DIC analysis. Figure 8-8 shows the image of the specimen and the overlaid strain profile obtained using DIC analysis at t=235 µs. The DIC analysis covers a length of approximately 25 mm along the specimen.

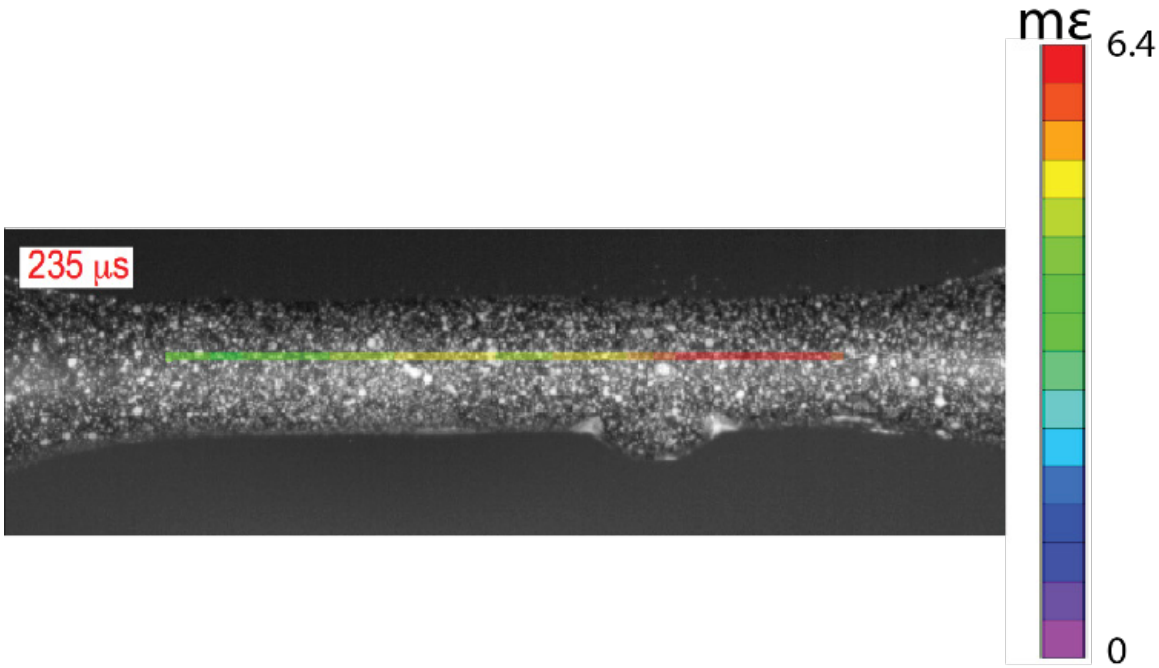

Figure 8-8. DIC imaging shows the strain profile along the Hopkinson bar specimen. This strain profile is shown by the overlaid color map at t=235 μs [11].

Figure 8-9 shows a comparison between the strain profile obtained at t=230 μs using an FBG and the profile at t=235 μs obtained using the DIC analysis. Since the grating used was only 10 mm long, the grating does not span the whole length of the 25 mm section analyzed from the DIC measurements. However, the 10 mm section that is overlapped (from about -3 mm to 7 mm) corresponds relatively well. This shows that the FBG is able to capture the strain profile along the specimen even without a direct line of sight.

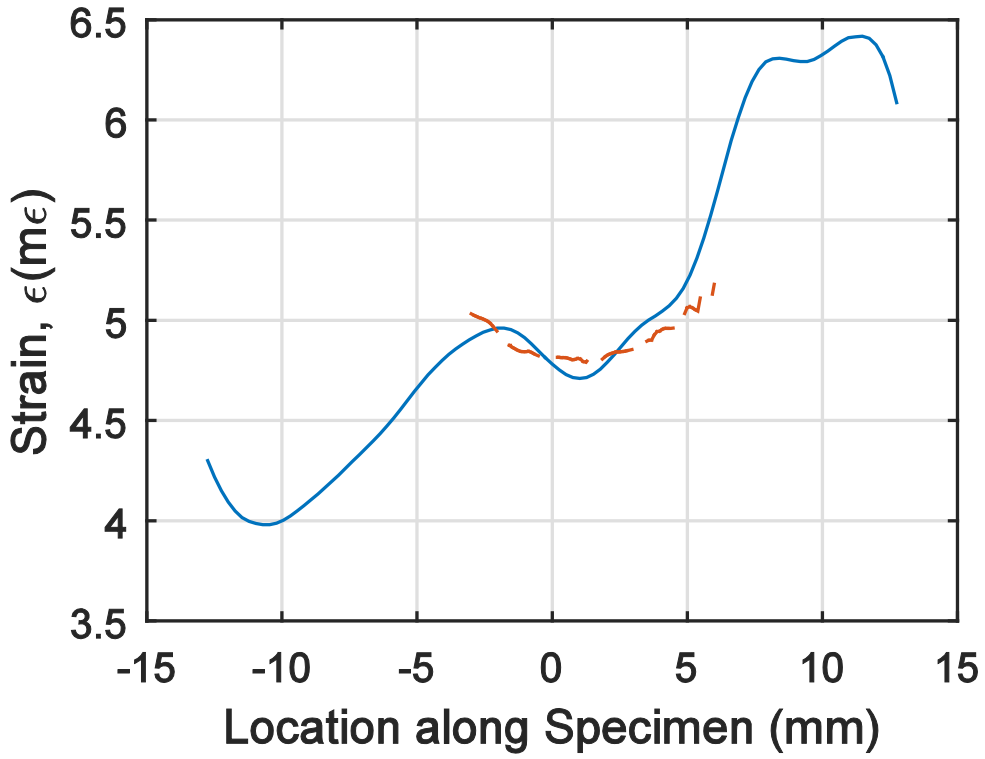

Figure 8-9. The strain profile obtained by the FBG (red, dashed) at t=230 μs resembles the strain profile obtained using the DIC measurements (blue) at t=235 μs [11].

Additionally, we are also able to record the average strain on the specimen by using the FBG. Figure 8-10 compares the strain measurements of the Hopkinson bar using 3 different approaches: strain gauges, DIC, and FBG measurements. The strain measured by the FBG correlates with the trends seen on the strain measurements found using the strain sensors and DIC analysis.

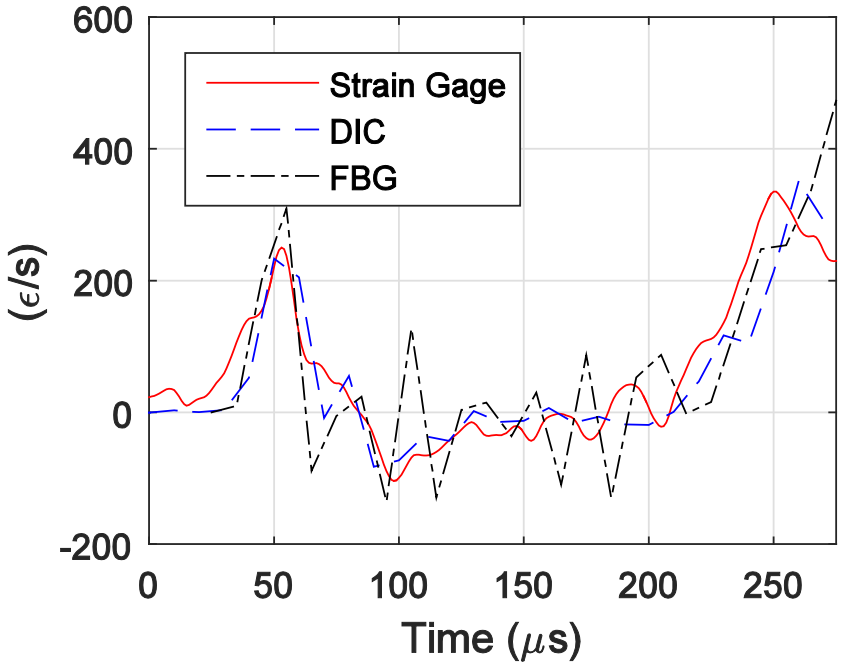

Figure 8-10. Averages strain over time across the tapered section of the split Hopkinson bar using three measurement methods: strain gauges (red), DIC (blue, dashed), and FBG (black, dotted-dashed) [11].

8.3 Conclusions

FBGs provide another method by which high dynamic strain rates can be measured. This is shown by measuring strain on a Hopkinson bar, while the strain profiles are obtained through optimization using the transfer matrix method. Not only do the FBGs provide a means by which the strain profile can be dynamically interrogated (with spectrum sampling rates of 100 kHz and above), they can do so without direct line of sight.

REFERENCES

1. Shumway, L., Stan, N., Seng, F., King, R., Selfridge, R., Schultz, S. (n.d.), "High voltage measurements using slab coupled optical sensors (SCOS)." *Review of Scientific Instruments (In Progress).*

2. Shumway, L., Stan, N., Seng, F., King, R., Selfridge, R., and Schultz, S. (2015, August). "High voltage measurements using slab coupled optical sensors (SCOS)." *Proceedings from 2015 IEEE 58th International Midwest Symposium on Circuits and Systems,* 1-4.

3. Shumway, L., Chadderdon, S., Powell, A., Li, A., Austin, D., Hawkins, A., Selfridge, R., and Schultz, S. (2014). "Ion trap electric field measurements using slab coupled optical sensors." *Proceedings of SPIE Smart Structures and Materials+ Nondestructive Evaluation and Health Monitoring, 9062*, 90620I-90620I.

4. Chadderdon, S., Shumway, L., Powell, A., Li, A., Austin, D., Hawkins, A., Selfridge, R., and Schultz, S. (2014). "Ion trap electric field characterization using slab coupled optical fiber sensors." *Journal of the American Society for Mass Spectrometry*, *25*(9), 1622-1627.

5. Seng, F., Stan, N., Josephson, C., King, R., Shumway, L., Selfridge, R., and Schultz, S. (2015). "Push–pull slab coupled optical sensor for measuring electric fields in a vibrational environment." *Applied optics*, *54*(16), 5203-5209.

6. Seng, F., Stan, N., Chadderdon, S., Josephson, C., King, R., Shumway, L., Selfridge, R., and Schultz, S. (2015, March). "Optical electric field sensor using push-pull for vibration noise reduction." *IEEE: Optical Fiber Communications Conference and Exhibition,* 1-3.

7. Seng, F., Stan, N., King, R., Josephson, C., Shumway, L., Hammond, A., Johnston, H., Velasco, I., and Schultz, S. (2016). Optical Sensing of Electric Fields in Harsh Environments. *Journal of Lightwave Technology.*

8. Seng, F., Stan, N., King, R., Worthen, R., Shumway, L., Selfridge, R., and Schultz, S. (2016, March). "Optical sensing of electrical fields in harsh environments." *IEEE: Optical Fiber Communications Conference and Exhibition,* 1-3.

9. Stan, N., Seng, F., Shumway, L., King, R., Selfridge, R., and Schultz, S. (2016). "High electric field measurement using slab-coupled optical sensors." *Applied optics*, *55*(3), 603-610.

10. Stan, N., Shumway, L., Seng, F., King, R., Selfridge, R., and Schultz, S. (2015, May). “High electric field measurement with slab coupled optical sensors using nonlinear calibration.” *SPIE Sensing Technology+ Applications*, 94800T-94800T.

11. Seng, F., Hackney, D., Goode, T., Shumway, L., Hammond, A., Shoemaker, G., Pankow, M., Peters, K., and Schultz, S. (2016). “Split Hopkinson bar measurement using high-speed full-spectrum fiber Bragg grating interrogation.” *Applied Optics*, *55*(25), 7179-7185.

12. King, R., Stan, N., Seng, F., Shumway, L., and Schultz, S. (2015, August). “Measuring arc dynamics using a slab coupled optical sensor (SCOS).” *2015 IEEE 58th International Midwest Symposium on Circuits and Systems (MWSCAS),* 1-4.

13. Stan, N., Seng, F., King, R., Shumway, L., Schultz, S. (n.d.) “Non-intrusive voltage measurement in a coaxial cable using slab-coupled optical fiber sensors.” *Applied Optics*. (*In Progress*).

14. Seng, F., Zhenchao, Y., King, R., Shumway, L., Stan, N., Hammond, A., Warnick, K., Schultz, S. (2017). "Slab coupled optical sensor (SCOS) directional sensitivity rerouting and enhancement using dipole antennas." *Applied Optics 56(*17), 4911-4916.

15. Halim, A. (1980). *High-voltage Measurement Techniques* (Doctoral dissertation). Retrieved from University of British Columbia.

16. Kuffel, J., and Kuffel, P. (2000). *High voltage engineering fundamentals*, Newnes.

17. Feser, K. (1971). "A new type of voltage divider for the measurement of high impulse and ac voltages." Haefely Publication E, 1-12. (in its own journal translated)

18. Mitra, S., Senthil, K., Singh, S., Kumar, R., and Sharma, A. (2016). “Development of a novel voltage divider for measurement of sub-nanosecond rise time high voltage pulses.” *Review of Scientific Instruments*, *87*(2), 024703.

19. Liu, Y., Lin, F., Hu, G., and Zhang, M. (2011). “Design and performance of a resistive-divider system for measuring fast HV impulse.” *IEEE Transactions on Instrumentation and Measurement*, *60*(3), 996-1002.

20. Bluhm, H. (2006). *Power Systems,* Springer.

21. Hebner, R., Malewski, R., and Cassidy, E. (1977). “Optical methods of electrical measurement at high voltage levels.” *Proceedings of the IEEE*, *65*(11), 1524-1548.

22. Kind, D. (2013). *An introduction to high-voltage experimental technique: textbook for electrical engineers*, Springer-Verlag.

23. Hylten-Cavallius, N., and Giao, T. (1969). “Floor net used as ground return in high-voltage test areas.” *IEEE Transactions on Power Apparatus and Systems*, (7), 996-1005.

24. Rahmatian, F., Chavez, P., and Jaeger, N. (2002). “230 kV optical voltage transducers using multiple electric field sensors.” *IEEE transactions on power delivery*, *17*(2), 417-422.

25. Santos, J., Taplamacioglu, M., and Hidaka, K. (2000). “Pockels high-voltage measurement system.” *IEEE Transactions on power delivery*, *15*(1), 8-13.

26. Kumada, A., and Hidaka, K. (2013). “Directly high-voltage measuring system based on Pockels effect.” *IEEE transactions on power delivery*, *28*(3), 1306-1313.

27. Miki, M., Rakov, V., Rambo, K., Schnetzer, G., and Uman, M. (2002). “Electric fields near triggered lightning channels measured with Pockels sensors.” *Journal of Geophysical Research: Atmospheres*, *107*(D16).

28. Hidaka, K. (1999). “Electric field and voltage measurement by using electro-optic sensor.” *Eleventh International Symposium on High Voltage Engineering.* 2(467), 1-14.

29. Sawa, T., Kurosawa, K., Kaminishi, T., and Yokota, T. (1990). “Development of optical instrument transformers.” *IEEE Transactions on Power Delivery*, *5*(2), 884-891.

30. Saleh, B., Teich, M. (2007). *Fundamentals of photonics - second edition*, John Wiley and Sons.

31. Prasad, P., and Williams, D. (1991). *Introduction to nonlinear optical effects in molecules and polymers,* John Wiley and Sons.

32. Chadderdon, S. (2014). *High-voltage Measurement Techniques* (Doctoral dissertation). Retrieved from University of British Columbia Application Improvements of Slab-Coupled Optical Fiber Sensors (Doctoral dissertation). Retrieved from Brigham Young University ScholarsArchive.

33. King, R., Seng, F., Stan, N., Cuzner, K., Josephson, C., Selfridge, R., and Schultz, S. (2016). “Slab-coupled optical sensor fabrication using side-polished Panda fibers.” *Applied optics*, *55*(31), 8848-8854.

34. King, R. (2016). *Voltage Measurement Using Slab-Coupled Optical Sensors with Polarization-Maintaining and Absorption-Reduction Fiber* (master’s thesis). Retrieved from Brigham Young University ScholarsArchive.

35. Gibson, R. (2009). *Slab-Coupled Optical Fiber Sensors for Electric Field Sensing* (Doctoral dissertation). Retrieved from Brigham Young University ScholarsArchive.

36. Gibson, R., Selfridge, R., Schultz, S., Wang, W., and Forber, R. (2008). "Electro-optic sensor from high Q resonance between optical D-fiber and slab waveguide." *Applied optics*, *47*(13), 2234-2240.

37. Chadderdon, S., Gibson, R., Selfridge, R., Schultz, S., Wang, W., Forber, R., Lou, J., and Jen, A. (2011). "Electric-field sensors utilizing coupling between a D-fiber and an electro-optic polymer slab." *Applied optics*, *50*(20), 3505-3512.

38. Gibson, R., Selfridge, R., and Schultz, S. (2009). "Electric field sensor array from cavity resonance between optical D-fiber and multiple slab waveguides." *Applied optics*, *48*(19), 3695-3701.

39. Kim, K., Kwon, H., Song, J., Lee, S., Jung, W., and Kang, S. (2000). Polarizing properties of optical coupler composed of single mode side-polished fiber and multimode metal-clad planar waveguide. *Optics communications*, *180*(1), 37-42.

40. Millar, C., Brierley, M., and Mallinson, S. (1987). Exposed-core single-mode-fiber channel-dropping filter using a high-index overlay waveguide. *Optics letters*, *12*(4), 284-286.

41. Yariv, A., and Yeh, P. (1984), *Optical waves in crystals*, John Wiley and Sons.

42. Ravindra, A., and Mosch, W. (2011). *High voltage and electrical insulation engineering*, John Wiley and Sons.

43. Wadhwa, C. (2007). *High voltage engineering*, New Age International.

44. Kok, J. (1961). *Electrical breakdown of insulating liquids*.

45. Schwab, A., and Pagel, J. (1972). "Precision capacitive voltage divider for impulse voltagge measurements." *IEEE Transactions on Power Apparatus and Systems*, (6), 2376-2382.

46. Pellinen, D., and Heurlin, S. (1971). "A nanosecond risetime megavolt voltage divider." *Review of Scientific Instruments*, *42*(6), 824-827.

47. Mesyats, G. (2007). *Pulsed power*, Springer Science and Business Media.

48. Inokuchi, M., Akiyama, M., Sakugawa, T., Akiyama, H., and Ueno, T. (2009, June). "Development of miniature Marx generator using BJT." *IEEE Transactions on Pulsed Power,* 57-60.

49. Yamada, C., Ueno, T., Namihira, T., Sakugawa, T., Katsuki, S., and Akiyama, H. (2007, June). "Evaluation of BJTs as closing switch of miniaturized Marx generator." *IEEE Transactions on Pulsed Power*, (1), 468-471.

50. Heeren, T., Ueno, T., and Akiyama, H. (2005, June). “Miniature, Solid-State, Kilovolt, Nanosecond Pulse Generator with Variable Pulse-Width, Pulse-Polarity, and Pulse Frequency.” *IEEE Transactions on Pulsed Power*, 1360-1363.

51. Wu, Y., Liu, K., Qiu, J., Liu, X., and Xiao, H. (2007). “Repetitive and high voltage Marx generator using solid-state devices.” *IEEE Transactions on Dielectrics and Electrical Insulation*, *14*(4).

52. Baek, J., Yoo, D., Rim, G., and Lai, J. (2005). “Solid state Marx generator using series-connected IGBTs.” *IEEE Transactions on plasma science*, *33*(4), 1198-1204.

53. Seng, F., Hackney, D., Goode, T., Shumway, L., Hammond, A., Shoemaker, G., Pankow, M., Peters, K., and Schultz, S. (2016). “Split Hopkinson bar measurement using high-speed full-spectrum fiber Bragg grating interrogation.” *Applied Optics*, *55*(25), 7179-7185.

54. Yariv, A. (1973). “Coupled-mode theory for guided-wave optics.” *IEEE Journal of Quantum Electronics*, *9*(9), 919-933.

55. Yamada, M., and Sakuda, K. (1987). “Analysis of almost-periodic distributed feedback slab waveguides via a fundamental matrix approach.” *Applied optics*, *26*(16), 3474-3478.

56. Prabhugoud, M., and Peters, K. (2004). “Modified transfer matrix formulation for Bragg grating strain sensors.” *Journal of lightwave technology*, *22*(10), 2302.

57. Peters, K., Studer, M., Botsis, J., Iocco, A., Limberger, H., and Salathé, R. (2001). “Embedded optical fiber Bragg grating sensor in a nonuniform strain field: measurements and simulations.” *Experimental Mechanics*, *41*(1), 19-28.

58. Gama, B., Lopatnikov, S., and Gillespie, J. (2004). “Hopkinson bar experimental technique: a critical review.” *Applied mechanics reviews*, *57*(4), 223-250.

59. Chen, W., Zhang, B., and Forrestal, M. J. (1999). “A split Hopkinson bar technique for low-impedance materials.” *Experimental mechanics*, *39*(2), 81-85.

60. Christensen, R., Swanson, S., and Brown, W. (1972). “Split-Hopkinson-bar tests on rock under confining pressure.” *Experimental Mechanics*, *12*(11), 508-513.